ADVANCES IN ATMOSPHERIC SCIENCES, VOL. 37, MAY 2020, 455–476

• Original Paper •

Atmospheric River Signatures in Radiosonde Profiles and Reanalyses at the Dronning Maud Land Coast, East Antarctica

Irina V. GORODETSKAYA*[1], Tiago SILVA[2], Holger SCHMITHÜSEN[3], and Naohiko HIRASAWA[4,5]

[1]*Centre for Environmental and Marine Studies (CESAM)*, *Department of Physics*, *University of Aveiro*, *Aveiro* 3810-193, *Portugal*

[2]*Department of Atmospheric and Cryospheric Sciences*, *University of Innsbruck*, *Innsbruck* 6020, *Austria*

[3]*Alfred Wegener Institute*, *Helmholtz Centre for Polar and Marine Research*, *Bremerhaven* 27570, *Germany*

[4]*National Institute of Polar Research*, *Tachikawa* 190-8518, *Japan*

[5]*SOKENDAI (Graduate University for Advanced Studies)*, *Hayama* 240-0193, *Japan*

(Received 2 November 2019; revised 29 February 2020; accepted 4 March 2020)

ABSTRACT

Atmospheric rivers (ARs) are an important component of the hydrological cycle linking moisture sources in lower latitudes to the Antarctic surface mass balance. We investigate AR signatures in the atmospheric vertical profiles at the Dronning Maud Land coast, East Antarctica, using regular and extra radiosonde measurements conducted during the Year of Polar Prediction Special Observing Period November 2018 to February 2019. Prominent AR events affecting the locations of Neumayer and Syowa cause a strong increase in specific humidity extending through the mid-troposphere and a strong low-level jet (LLJ). At Neumayer, the peak in the moisture inversion (up to 4 g kg^{-1}) is observed between 800 and 900 hPa, while the LLJ (up to 32 m s^{-1}) is concentrated below 900 hPa. At Syowa the increase in humidity is less pronounced and peaks near the surface, while there is a substantial increase in wind speed (up to 40 m s^{-1}) between 825 and 925 hPa. Moisture transport (MT) within the vertical profile during the ARs attains a maximum of 100 g kg^{-1} m s^{-1} at both locations, and is captured by both ERA-Interim and ERA5 reanalysis data at Neumayer, but is strongly underestimated at Syowa. Composites of the enhanced MT events during 2009–19 show that these events represent an extreme state of the lower-tropospheric profile compared to its median values with respect to temperature, humidity, wind speed and, consequently, MT. High temporal- and vertical-resolution radiosonde observations are important for understanding the contribution of these rare events to the total MT towards Antarctica and improving their representation in models.

Key words: Antarctica, moisture transport, radiosonde observations, YOPP-SOP-SH, reanalysis

Citation: Gorodetskaya, I. V., T. Silva, H. Schmithüsen, and N. Hirasawa, 2020: Atmospheric river signatures in radiosonde profiles and reanalyses at the Dronning Maud Land coast, East Antarctica. *Adv. Atmos. Sci.*, **37**(5), 455–476, https://doi.org/10.1007/s00376-020-9221-8.

Article Highlights:

- Atmospheric river signatures are prominent in vertical profiles at the East Antarctic coast as shown by radiosonde observations and reanalysis data.
- Enhanced moisture transport is driven by the low-level jet and humidity maximum, which show decoupling at the Antarctic coast.
- ERA5 is better at representing atmospheric rivers compared to ERA-Interim at Neumayer, while both underestimate atmospheric-river moisture transport at Syowa.

1. Introduction

The Antarctic continent is a highly complex and critically important component of the global climate system that remains poorly understood, especially due to data-sparse and remote regions with difficult human access. Precipitation over the Antarctic ice sheet is dependent on the poleward moisture transport (MT) from lower latitudes, which is mostly accomplished by exratropical cyclones reaching Antarctica (e.g., Bromwich et al., 1995; Tsukernik and Lynch, 2013; Sinclair and Dacre, 2019). Some of these extratropical cyclones [sometimes multiple cyclones, as demonstrated by Sodemann and Stohl (2013) for the Arctic] are asso-

* Corresponding author: Irina V. GORODETSKAYA
Email: irina.gorodetskaya@ua.pt

ciated with atmospheric rivers (ARs)—long, narrow and transient corridors of enhanced vertically integrated water vapor (IWV) and horizontal vapor transport (IVT) typically within the cyclones' warm conveyor belt, ahead of the cold front (Ralph et al., 2004; Cordeira et al., 2017). ARs are typically associated with low-level jets (LLJ) (Ralph et al., 2004) and can strongly interact with the local barrier jets (Ralph et al., 2016). The moisture supply feeding ARs is found to be frequently linked to the exports of tropical moisture, which makes ARs outstanding features in terms of the amount of moisture they carry compared to other cyclones not characterized by ARs (Knippertz et al., 2013). Nash et al. (2018) showed that, annually, ARs contribute more than 90% of the poleward MT in the middle to high latitudes. The authors used a global AR algorithm developed by Guan and Waliser (2015) to confirm the original conclusions for the Southern Hemisphere MT by ARs reached by Zhu and Newell (1998). In Antarctica, high-precipitation events associated with ARs reaching the ice sheet have been found to be an important component of the hydrological cycle linking moisture sources in lower latitudes to Antarctic precipitation (Gorodetskaya et al., 2014). Such extreme precipitation events play a dominant role in the variability of Antarctic snowfall (Turner et al., 2019). Recent studies have also highlighted the role of ARs in warming/melt events in Antarctica (Bozkurt et al., 2018; Wille et al., 2019). Thus, poleward heat and MT via ARs can strongly affect the total ice-sheet mass balance and its input to global sea-level rise.

Poleward MT at the Antarctic coastal region determines the total amount of precipitation over the ice sheet. Previous studies have investigated the climatological MT budget (Bromwich et al., 1995; Connolley and King, 1993) and its temporal variability (Dufour et al., 2019) at the Antarctic coast using reanalysis data as well as radiosonde observations. Nygård et al. (2013) used radiosonde data to demonstrate the persistence of the near-surface humidity inversions at the coastal regions of Antarctica—typically less than 200 m deep and 0.2 g kg^{-1} strong—with approximately 60% being accompanied by horizontal advection of water vapor. The fine structure of the troposphere in the first 3 km above the ground was examined by Vignon et al. (2019) using radiosonde data at the East Antarctic coastal and escarpment region stations and compared to reanalysis products and regional climate model results, demonstrating the important role of the katabatic wind in the temperature and relative humidity (RH) profiles. These previous studies investigated the average MT and amounts without distinguishing the role of extreme values. As studies on the impact of ARs in Antarctica point towards the important contribution of ARs with respect to heat and moisture inputs over the ice sheet (Gorodetskaya et al., 2014; Bozkurt et al., 2018; Wille et al., 2019), it is important to explore the vertical structure associated with such events and the controlling factors for enhanced MT. Previous studies have also pointed out the important coupling of the synoptic-scale atmospheric circulation, orographic blocking and katabatic forcing in creating strong LLJs along the ice-sheet coastal areas (Parish, 1983; Parish and Bromwich, 2007; Seefeldt and Cassano, 2008; Yamada and Hirasawa, 2018), and their behavior during the landfall of ARs in Antarctica is still to be explored.

Our work investigates vertical profiles of humidity, temperature, wind and MT at high temporal and vertical resolution, focusing on the extreme values of MT, which characterize the ARs. For this purpose, we use unprecedented high-frequency radiosonde measurements available during the Year of Polar Prediction (YOPP) special observing period (SOP) in the Southern Hemisphere (SH) during November 2018 to February 2019. Different YOPP SOPs were carried out at both polar regions as a flagship activity of the Polar Prediction Project (Jung et al., 2016). Our focus is on the coastal region of Dronning Maud Land (DML), East Antarctica, which has experienced anomalously high snow accumulation in recent years (Boening et al., 2012; King et al., 2012; Lenaerts et al., 2013) owing to rare intense snowfall events linked to ARs (Gorodetskaya et al., 2014). Specifically, we use observations from two stations—Neumayer and Syowa—located at the coast near the longitudinal margins of the DML (8°W and 39°E, respectively). National programs run at these stations have a long record of radiosonde observations and both contributed to YOPP SOP-SH with more frequent radiosonde observations and other measurements (Hirasawa, 2017; Schmithüsen et al., 2017). Results obtained for the YOPP SOP-SH period are compared to a longer period (2009–19) using regular long-term radiosonde measurements at both stations available via the Integrated Global Radiosonde Archive, version 2 (IGRA2). The aim of our study is to: (1) identify and analyze ARs affecting DML during YOPP SOP-SH, and specifically those affecting Neumayer and Syowa stations; (2) analyze vertical profiles from radiosondes at the two stations during the ARs using frequent launches during YOPP SOP-SH; (3) study their association with the presence of LLJs and moisture inversions; (4) put the YOPP SOP-SH AR events in perspective with the longer-term record of enhanced MT events using the IGRA2 dataset; and (5) evaluate AR representation in reanalysis products.

2. Station environment and weather regimes

The analysis focuses on the DML coastal region and is based on radiosonde data from two Antarctic research stations—Neumayer and Syowa (see Fig. 1 for their locations). Neumayer (70°39'S, 8°15'W) is situated on the Ekström ice shelf, about 5 km from the southwest part of Atka bay, 43 m above mean sea level (MSL) (König-Langlo et al., 1998; König-Langlo and Loose, 2007). The radiosonde launch site is located on the roof of the main station building, 25 m above the surrounding snow level, and hence 68 m MSL (Schmithüsen and Müller, 2019a, 2019b, 2019c). The Ekström ice shelf is oriented north–south, has a length of about 100 km, and a total area of some 6000 km^2. The ice shelf is characterized by a homogenous flat surface, sloping gently upward to the south [inclination: ~40 m $(100\ km)^{-1}$]

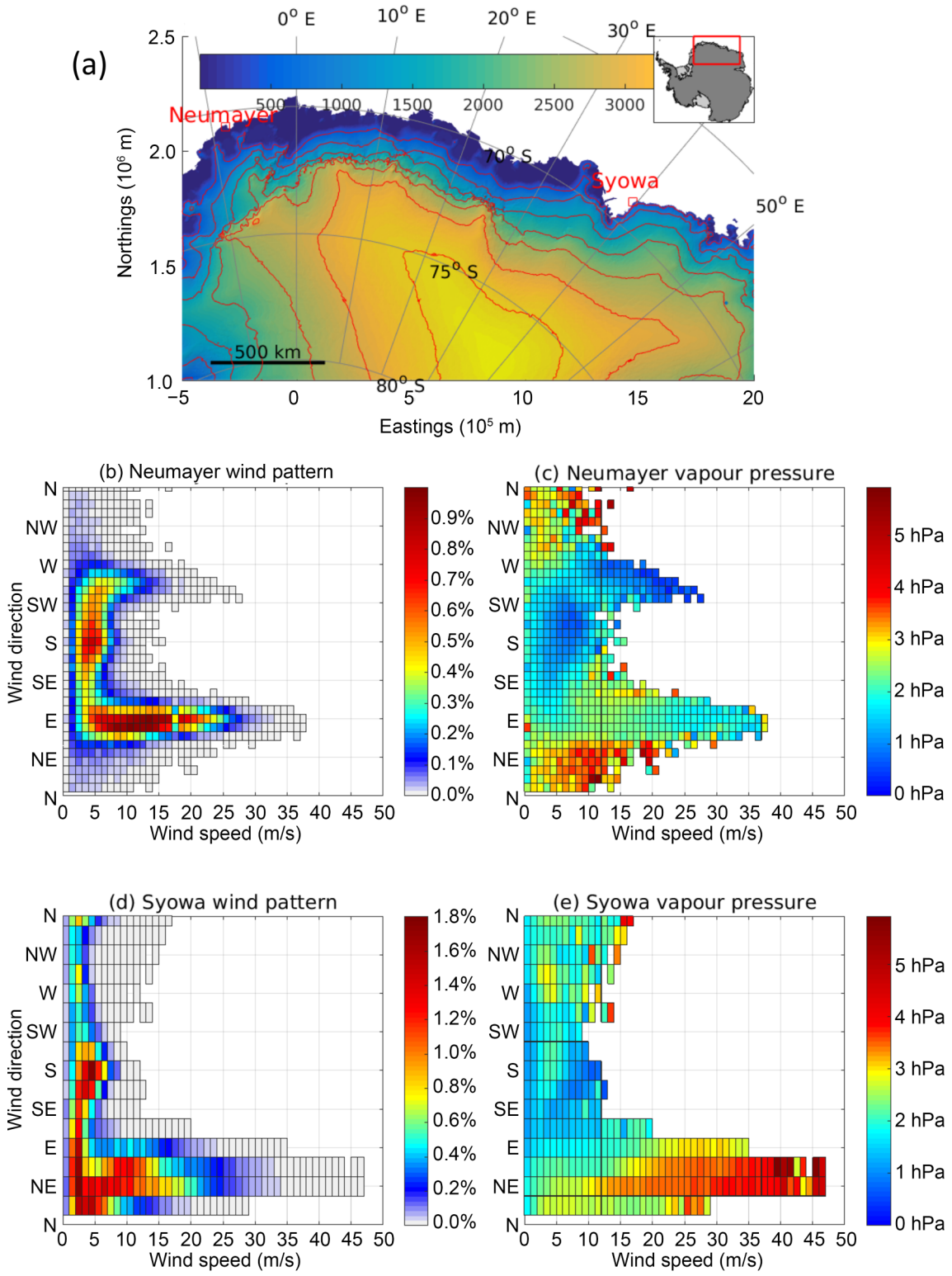

Fig. 1. Regional map and wind-humidity regimes for Neumayer and Syowa: (a) ice surface elevation map (color shading; units: m) from Bedmap2 (Fretwell et al., 2013) for the extended DML region (zoomed area over the Antarctic continent shown in the upper-right corner); red squares show the locations of Neumayer and Syowa stations. (b) Wind direction versus wind speed (units: m s^{-1}), with colors indicating the frequency of occurrence (number of observations per bin relative to total number of synoptic observations; units: %). (c) Water vapor pressure (colors; units: hPa) for each wind speed–direction combination at Neumayer. (d, e) As in (b, c) but for Syowa. At Neumayer, based on three-hourly measurements from 1 January 1981 to 31 December 2019 (Schmithüsen, 2020). At Syowa, based on hourly measurements from 1 January 1994 to 31 December 2019 (Yamanouchi et al., 2020).

(Thyssen and Grosfeld, 1988). Neumayer is located on the southern edge of the circumpolar trough and is frequently affected by cyclonic disturbances all year round.

The weather at Neumayer station is dominated by two regimes, which can be seen in the wind and absolute humidity analysis in Figs. 1b and c (see Appendix for methods). First, the topography of the Ekström ice shelf and its surroundings causes southerly katabatic winds of low to moderate magnitude (typically 5 m s^{-1}, rarely more than 10 m s^{-1}; Fig. 1b) and mostly clear-sky and dry conditions (Fig. 1c). The MT at Neumayer during these weather situations is small and is mostly due to surface and drifting snow sublimation and moisture trapping in the stable boundary layer (Bintanja, 2000; Lenaerts et al., 2010). This southerly-wind regime is occasionally extended to southwesterly to westerly wind directions, also with dry conditions but stronger wind speeds (Figs. 1b and c). This regime is typically associated with a high-pressure ridge reaching rather deep into the Weddell Sea, causing moderate southwesterly to westerly winds of typically no more than 20 m s^{-1} and transporting little moisture.

The second important weather regime is characterized by extratropical cyclones moving from the northern Weddell Sea eastwards. These low-pressure systems, together with the orographic steering caused by the rising Antarctic ice-sheet topography south of Neumayer, induce strong easterly winds at Neumayer's location [Fig. 1b and Klöwer et al. (2013)]. The topography forces the flow to often be straight easterly (90°), varying only gently between 70° and 110°. These winds associated with extratropical cyclones advect heat and moisture (Fig. 1c) and typically cause increased temperatures and snowfall. Particularly, synoptic observations at Neumayer classifying "moderate" or "heavy" snowfall [according to WMO (2011b)] have been frequently reported during these low-pressure systems. Wind speeds during cyclonic disturbances frequently exceed 25 m s^{-1} (Fig. 1b) and can cause heavy blowing-snow and whiteout events (Gossart et al., 2017). There are infrequent occurrences of moderate northeasterly winds (up to 10–15 m s^{-1}) near the surface associated with the blocking high penetrating into the coastal area (and the wind direction changing to northwesterly with height), which causes high precipitation (snowfall) events on rare occasions (Schlosser et al., 2010). AR events discussed in this study belong to this category—northeasterly winds of moderate magnitude near the surface and high humidity values (Figs. 1b and c).

On rare occasions during summer, precipitation can also be in the form of drizzle and rainfall [see "Forecasting at specific locations" for Neumayer station in Turner and Pendlebury (2004)], which is important for the local surface mass balance. During summer months, there is an occurrence of surface snowmelt (on average 50 mm water equivalent during the summer season, with large interannual variability), which also significantly influences surface energy and the mass budget (Jakobs et al., 2019). Generally, situations of low pressure gradients can cause fog development around Neumayer. There are also occurrences of sea smoke when cold katabatic winds blow over the warm open water (Turner and Pendlebury, 2004).

Syowa Station (69.08°S; 39.68°E; 15 m MSL) is located on Ongul Island about 4 km away from the east coast of the Lützow-Holm bay. The launching position of the radiosondes is (69.00°S, 39.58°E) at 22 m MSL. The prevailing winds at Syowa Station are northeasterly, reflecting the influence of katabatic winds blowing along the topography (Sato and Hirasawa, 2007). This wind regime is characterized by a large range of wind speeds, with the most frequent between near-zero to 15 m s^{-1}, and occasionally exceeding 45 m s^{-1} (Fig. 1d). The average annual wind speed is about 5 m s^{-1}, and blizzards occur on average about 25 times a year, during which the wind speeds range from 15 to 40 m s^{-1} (Sato and Hirasawa, 2007). A remarkable event on 17 January 2015, when wind gusts attained 51 m s^{-1}, was studied in detail by Yamada and Hirasawa (2018). The authors showed that such strong winds were generated in the presence of a synoptic-scale depression by the mechanism of orographic blocking. As shown in Figs. 1d and e, in the northeasterly to easterly wind direction, the most frequent moderate wind speeds correspond to low humidity values, while high wind speeds attain maximum vapor pressure. A secondary peak in the wind-regime frequency is observed for southerly to southeasterly wind directions (Fig. 1d), corresponding to very dry conditions (Fig. 1e). While the northeasterly to easterly wind regime can be a mixture of mechanisms, including both katabatic and synoptic processes, the southerly to southeasterly wind regime can be attributed mostly to katabatic flow (Sato and Hirasawa, 2007). Snowfall at Syowa station is typically associated with synoptic-scale low-pressure systems (e.g., Konishi et al., 1998), which are commonly accompanied by high wind speeds that cause blizzards.

3. Data and methods

3.1. *Radiosonde data*

3.1.1. *Radiosonde sensors and measurement uncertainties*

Radiosondes from two different manufacturers are used at the Neumayer and Syowa stations—Vaisala (Finland) and Meisei Electric (Japan). Syowa station was certified by the WMO in 2018 as a station that meets the requirements of GRUAN (the Global Climate Observing System Reference Upper-Air Network; https://www.gruan.org) and the Meisei RS-11G radiosonde was certified as a radiosonde for the purpose of GRUAN (Kizu et al., 2018). Recent changes in radiosonde types during the period used in this study (2009–19) are as follows: RS11G since February 2018; RS06G from 12 March 2013 to January 2018; and RS01G from February 2008 to 11 March 2013.

At Neumayer station, the regularly used radiosonde type during 2009–18 was Vaisala RS92-SGP, which was changed to Vaisala RS41-SGP on 1 June 2018. The manufacturer claims enhanced performance of temperature and humid-

ity sensors by the RS41 type. Thorough testing of the transition from RS92 to RS41 sondes was performed within GRUAN (Jensen et al., 2016; Kawai et al., 2017). At Neumayer station the transition is controlled by a 2-yr period (July 2018 to July 2020) of weekly tandem launches. Thus, radiosonde data available during the YOPP SOP-SH period are based on Vaisala RS41-SGP at Neumayer, and Meisei-RS11G at Syowa.

All radiosonde sensors have time-lag errors; few operational radiosonde types apply lag corrections, and the WMO does not define any variable to report if a lag correction is applied (Sun et al., 2013). The more severe the weather, the fewer points are recorded by the device, which is important when analyzing ARs typically characterized by high winds. Also, radiosonde launches might fail or be skipped totally during severe weather events due to high winds. At Neumayer station launches are possible at surface wind speeds up to 25 m s^{-1}, but launches might fail at lower wind speed as well. Consequently, data gaps exist, particularly during intense low-pressure systems located off the Antarctic coast, and especially during ARs associated with strong winds and, frequently, blizzards.

Below we provide a summary of humidity biases known in radiosonde measurements. Due to the complexity of these biases, we do not apply a possible uncertainty range in our analysis. Humidity data from the radiosondes are known to suffer from the so-called daytime solar radiation dry bias (Tomasi et al., 2006; Rowe et al., 2008). Humidity bias increases substantially at cold temperatures. The RS-92 model used at Neumayer station prior to 1 June 2018 has been shown to be slightly affected by common dry biases at cold temperatures, while the RS41 sensor might exhibit a slight wet bias in the troposphere (Kawai et al., 2017). The dry layers above the humidity inversion can also be problematic. As discussed in the report by Ingleby (2017), because of the longer response time of the humidity sensors compared to the temperature sensors, the dew point can be overestimated above the moisture inversion layers, followed by the sensor's recovery with more realistic dry values at higher altitudes.

The humidity sensor on the radiosonde Meisei series RS-11G used at Syowa station is a thin-film capacitive sensor. According to Kizu et al. (2018), these sensors give the total uncertainty in RH at around 4% in the troposphere. Analysis by Kobayashi et al. (2019) of dual flights of Meisei RS-11G with other sensors showed that RS-11G measurements of RH were, on average, 2% lower than those of Vaisala RS92-SGP under 90%–100% RH conditions, while RS-11G gave on average 5% higher values than RS92-SGP under RH < 50% conditions. The results from dual flights of RS-11G and a cryogenic frost-point hygrometer (CFH) (Vömel et al., 2007) also showed that RS-11G measurements of RH are 1%–10% higher than the CFH in the troposphere (Sugidachi and Fujiwara, 2013).

3.1.2. *YOPP radiosonde measurements*

During the austral summer season of 2018–19 (from 15 November 2018 to 15 February 2019), SOP-SH, as part of YOPP, was conducted at several stations by national Antarctic programs. Additional measurements during the SOP-SH period at Neumayer are described by Schmithüsen et al. (2017). At Neumayer, four radiosondes per day were launched during YOPP SOP-SH (at launch times of 0500, 1100, 1700, and 2300 UTC). The radiosonde launch times were typically one hour prior to the WMO main synoptic hours (which is the target time for the radiosonde to reach the 100 hPa level at an average ascent rate of ~5 m s^{-1}). Several gaps were present during the YOPP SOP-SH period, mainly due to high surface wind speeds (ten days with three launches per day, five days with two launches per day, and one day with only one launch).

Additional measurements during YOPP SOP-SH at Syowa station are described by Hirasawa (2017). At Syowa station there were three radiosonde launches daily (at launch times of 0500, 1100, and 2300 UTC) from 15 November to 31 December and 1–15 February. During January 2019, four daily radiosondes were launched (at launch times of 0500, 1100, 1700, and 2300 UTC). During 15 and 17 November there was only one launch per day, at 2300 UTC. At both stations, several gaps occurred during the AR events with severe weather conditions.

For our analysis of individual AR events, we use raw radiosonde measurements at high vertical resolution (1 hPa or less).

3.1.3. *IGRA2*

Further, for long-term analysis of enhanced MT events at both stations, we use radiosonde data available via IGRA2 (Durre et al., 2016). The IGRA2 dataset includes vertical profiles of temperature, humidity, wind speed and direction, atmospheric pressure, and geopotential height. In the IGRA2 dataset, a comprehensive set of quality-control procedures is applied to all radiosonde data to remove large errors, including: (1) validation of position and date/time; (2) removal of outliers exceeding the physically possible limits; (3) removal of data points where unrealistic thermal stratification was unstable; (4) removal of data points where pressure was not decreasing strictly monotonically; (5) removal of data points where RH exceeded 100% with respect to ice. The latter correction can result in the underestimation of events with increased humidity due to supersaturation conditions (Gettelman et al., 2006). However, our individual profile analysis during AR events showed that small supersaturation (typical for the events considered here) are kept in the profile. Durre et al. (2008) and Durre and Yin (2008) provided details about derived parameters and quality control applied to IGRA2 radiosonde data.

Here, we use the data containing all standard levels until 300 hPa [1000, 925, 850, 700, 500, 400, and 300 hPa (WMO, 2011a)] and all available additional levels (annual median vertical resolution available via IGRA2 archive is 230 m for Neumayer and 340 m for Syowa). We base our analysis on the period from 1 January 2009 until 8 October 2019 (the last available day in IGRA data at the moment of

analysis). This period was chosen in order to take into account the years with anomalously high snow accumulation at DML (2009 and 2011) associated with ARs (Gorodetskaya et al., 2014). Also, this is a period when higher quality humidity measurements are available due to using new sensors (see section 3.1.1). During 2009–19, radiosondes were regularly launched once per day, at 1200 UTC, at Neumayer station (which is also local time), and twice per day, at 0000 and 1200 UTC, at Syowa station (local time UTC+3). According to Ferreira et al. (2019), Neumayer and Syowa stations have an acceptable completeness of radiosonde observations for our analysis. Because of the low temporal resolution of regular radiosonde observations and reduced vertical resolution available via IGRA2, these data can be used only for detecting large-scale features and not for detailed analysis of small-scale variability. We use IGRA2 data for the 10-yr period analysis for consistency of the applied quality checks between the two stations. For our composite analysis the data were interpolated to 5-hPa height steps.

3.2. *AR algorithm*

In order to identify ARs impacting the extended DML region, an AR algorithm developed by Gorodetskaya et al. (2014) was applied with several modifications. In the first step of the algorithm a threshold is applied to the IWV (see Appendix) with integration from the near-surface pressure to 300 hPa. Both in Gorodetskaya et al. (2014) and Wille et al. (2019), IWV is computed between 900 and 300 hPa in order to avoid the strong near-surface katabatic flow. This transition from the katabatic outward flow to the inland advection at higher levels is shown in modeling studies (van Lipzig and van den Broeke, 2002) and demonstrated by reanalysis and radiosonde monthly mean observations (Dufour et al., 2019). Here, we extend the IWV integration to the first near-surface-level pressure equal to or less than 1000 hPa measured by radiosondes or available in reanalysis profiles in order to re-examine the contribution of the near-surface-layer humidity and wind at heights below 900 hPa to the inland MT during the ARs at the Antarctic coast.

The IWV at each grid point and time step is compared to the zonal-mean threshold depending on the saturated IWV (IWV_{sat}). The IWV_{sat} is a vertical integral of the saturated specific humidity (q_{sat}) profile, where q_{sat} is calculated from saturation vapor pressure as a function of the temperature profile using the Clausius–Clapeyron relationship (see Appendix). The IWV anomalies are defined using a threshold as described by Gorodetskaya et al. (2014):

$$IWV \geqslant IWV_{sat,mean} + AR_{coef}\,(IWV_{sat,max} - IWV_{sat,mean})\ ,$$

where $IWV_{sat,mean}$ is the zonal-mean IWV_{sat} along each latitude, $IWV_{sat,max}$ is the maximum value along the same latitude, and AR_{coef} (equal to 0.2) is a coefficient determining the relative strength of an AR. For details about parameter choice, see Gorodetskaya et al. (2014). Thus, in this AR algorithm both the enhanced heat and moisture poleward advection associated with the ARs are taken into account and excess IWV is compared to the reduced moisture saturation capacity of the polar atmosphere due to colder air temperatures compared to lower latitudes. At the same time, moisture advection within an AR is coincident with heat advection, which increases the difference between the IWV within an AR and mean IWV_{sat} along the same latitude determining the threshold for the IWV. Such an approach, taking into account the moisture-holding capacity of the atmosphere, is expected to better capture AR extensions and impacts in the cold polar atmosphere, while it can be problematic using absolute thresholds [see Shields et al. (2018) for various classes of AR algorithms participating in the Atmospheric River Tracking Method Intercomparison Project (ARTMIP)]. The percentile method showed good agreement with the algorithm used in this study for prominent events affecting the Antarctic Peninsula and West Antarctic Ice Sheet (Wille et al., 2019). A more in-depth comparison of polar-oriented algorithms and global algorithms as applied to Antarctica is under way as part of ARTMIP.

After applying the threshold, potential AR (pAR) objects are identified, and those pARs that are intersecting the Antarctic coastline are further subject to geometric criteria. Consecutive grid points where pARs intersect the Antarctic coast are used to calculate the pAR mean landfall location, from which only the objects extending northward by at least 20° latitude within a sector of 40° longitude wide (that is ±20° from the pAR mean landfall longitude) are considered as ARs. The longitude width of 40° is larger compared to the 30° width used by Gorodetskaya et al. (2014) in order to include pAR objects curving in the zonal direction. For pAR objects that meet the minimum geometrical criteria, the entire pAR object is identified as an AR and is tracked at each time step while the landfall points are present. By this, the AR presence at a particular time step is extended to an AR event that can last from several hours to more than one day.

3.3. *Reanalysis products and backward trajectories*

In this study, the input parameters used in the AR algorithm (vertical profiles of temperature and specific humidity at pressure levels) are taken from the ERA-Interim reanalysis dataset (Dee et al., 2011) interpolated to 0.25° spatial resolution (from the original 0.75° resolution) with six-hourly fields. ERA-Interim data were produced using 4D-Var (four-dimensional variational) data assimilation in the CY31r2 release of the ECMWF Integrated Forecast System (IFS) model, with 60 levels in the vertical direction from the surface up to 0.1 hPa. ERA-Interim has been extensively used for analysis and as regional climate model forcing data, particularly over Antarctica. Its production ceased in August 2019, and it is has since been replaced by ERA5 (Hersbach et al., 2019). ERA5 is produced using 4D-VAR data assimilation in the CY41r2 release of the ECMWF IFS, with 137 hybrid sigma/pressure levels in the vertical direction, the top level at 0.01 hPa, and at a 31-km horizontal resolution. We compare radiosonde profiles to both the ERA-

Interim and ERA5 reanalysis products.

We also apply backward trajectory analysis using the Hybrid Single-Particle Lagrangian Integrated Trajectory (HYSPLIT) model, version 4.1.0 (Stein et al., 2015), using an isentropic vertical motion method. Input meteorological fields are from the Global Data Assimilation System at a horizontal resolution of 1°. The air parcels were released in the grids containing the station locations [centered at (70.65°S, 8.25°W) for Neumayer and at (69.08°S, 39.68°E) for Syowa], at 500 m MSL, at the AR landfall time, and were tracked back during 72 hours. The trajectory ensemble option was chosen for analysis, starting multiple trajectories from the first selected starting location.

4. Results

4.1. *Prominent AR events at Neumayer and Syowa during YOPP*

The AR algorithm was run for the period November 2018 to February 2019 for the longitudinal sector spanning from 60°W (approximately at the Antarctic Peninsula/western edge of the Weddell Sea) to 90°E. In total, ten AR events with landfall within this extended DML sector were detected during November 2018 to February 2019 (period of YOPP-SOP-SH). There were four ARs in November, three in December, two in January, and one in February. Only two AR events affected Syowa's location. The other eight events had their landfall in the western part of DML, from which only two were in the vicinity of Neumayer. For our analysis, we have chosen the two most prominent AR events (lasting for at least one day) that affected the Neumayer and Syowa sites and had minimal data gaps (which are still present due to severe weather conditions during ARs).

Table 1 lists the reanalysis and radiosonde timings corresponding to each identified AR step. The spatial distribution of IWV together with mean sea level pressure (MSLP), and their temporal evolution together with the AR contours, are shown in Fig. 2. The AR landfall longitude shows the mean longitude at which the AR crossed the Antarctic coast, together with its extension expressed as minimum and maximum longitudes (Table 1). In the table we also provide the corresponding IVT and IWV (from near the surface up to 300 hPa) calculated based on the radiosonde profiles as well as ERA-Interim and ERA5 reanalysis data.

The Syowa AR event lasted from 1200 UTC 16 November until 1200 UTC17 November, with a mean landfall longitude ranging from 32°E to 43°E (Table 1, Fig. 2a). Radiosonde measurements showed an increase in the IWV up to 9 kg m^{-2} and an IVT up to 192 kg m^{-1} s^{-1} (at 0000 UTC 17 November), compared to the monthly median values (5.7 kg m^{-2} and 45 kg m^{-1} s^{-1}, respectively) and exceeding the 98th percentiles for the month of November (7.4 kg m^{-2} and 180 kg m^{-1} s^{-1}, respectively). The AR event at Neumayer was identified during 18 December 2018 from 0000 UTC to 1800 UTC, with a mean landfall longitude at 20°–22°W (Table 1, Fig. 2b). Radiosonde measurements showed a maximum increase in IWV up to 15 kg m^{-2} and an IVT up to 340 kg m^{-1} s^{-1}. This is a significant increase compared to the monthly median values (4.1 kg m^{-2} and 37.5 kg m^{-1} s^{-1}, respectively), exceeding the 98th percentiles for the month of December (12.6 kg m^{-2} and 270 kg m^{-1} s^{-1}, respectively).

The relatively weak peak values of IVT during these AR events at the two Antarctic stations point to a lower atmospheric moisture-holding capacity and problematic use of AR algorithms based on the absolute threshold of IVT [typically at least 250 kg m^{-1} s^{-1}; see Shields et al. (2018)] and fixed AR scales (Ralph et al., 2019) when applied in polar

Table 1. List of the AR time steps for two prominent AR events with landfall at the East Antarctic coast within the 60°W–90°E longitudinal sector identified during the YOPP SOP-SH period at the sites of Syowa and Neumayer. The columns give (1) AR event timings based on six-hourly time steps of the ERA-Interim reanalysis data, (2) AR landfall location—mean longitude and total extent (east/west longitudes) and mean latitude, (3) timings of the radiosonde launches corresponding to the AR events [the launch time is normally 1 h prior to the reanalysis hour given in column (1)], (4) corresponding IWV, and (5) IVT for Syowa and Neumayer calculated from radiosondes/ERA-Interim/ERA5.

(a) AR event affecting Syowa on 16–17 November 2018

AR events timings	AR landfall longitude (mean/east/west)/latitude	Radiosonde times	IWV (kg m^{-2})	IVT (kg m^{-1} s^{-1})
1200 UTC 16 Nov	34°E/32°E/36°E/68°S	1100 UTC 16 Nov	7/7/7	43/40/50
1800 UTC 16 Nov	43°E/32°E/54°E/67°S	no data	–/7/8	–/82/102
0000 UTC 17 Nov	39°E/31°E/48°E/68°E	2300 UTC 16 Nov	9/9/9	192/163/183
0600 UTC 17 Nov	40°E/30°E/50°E/68°E	no data	–/9/9	–/185/195
1200 UTC 17 Nov	32°E/26°E/37°E/69°S	no data	–/9/9	–/154/184

(b) AR event affecting Neumayer on 18 December 2018

AR events timings	AR landfall longitude (mean/east/west)/latitude	Radiosonde times	IWV (kg m^{-2})	IVT (kg m^{-1} s^{-1})
0000 UTC 18 Dec	20°W/34°W/6°W/74°S	2300 UTC 17 Dec	12/12/13	177/184/199
0600 UTC 18 Dec	21°W/38°W/4°W/74°S	0400 UTC 18 Dec	13/13/14	221/222/235
1200 UTC 18 Dec	22°W/40°W/3°W/74°S	no data	–/14/14	–/268/283
1800 UTC 18 Dec	21°W/40°W/2°W/74°S	1700 UTC 18 Dec	15/15/16	340/330/343

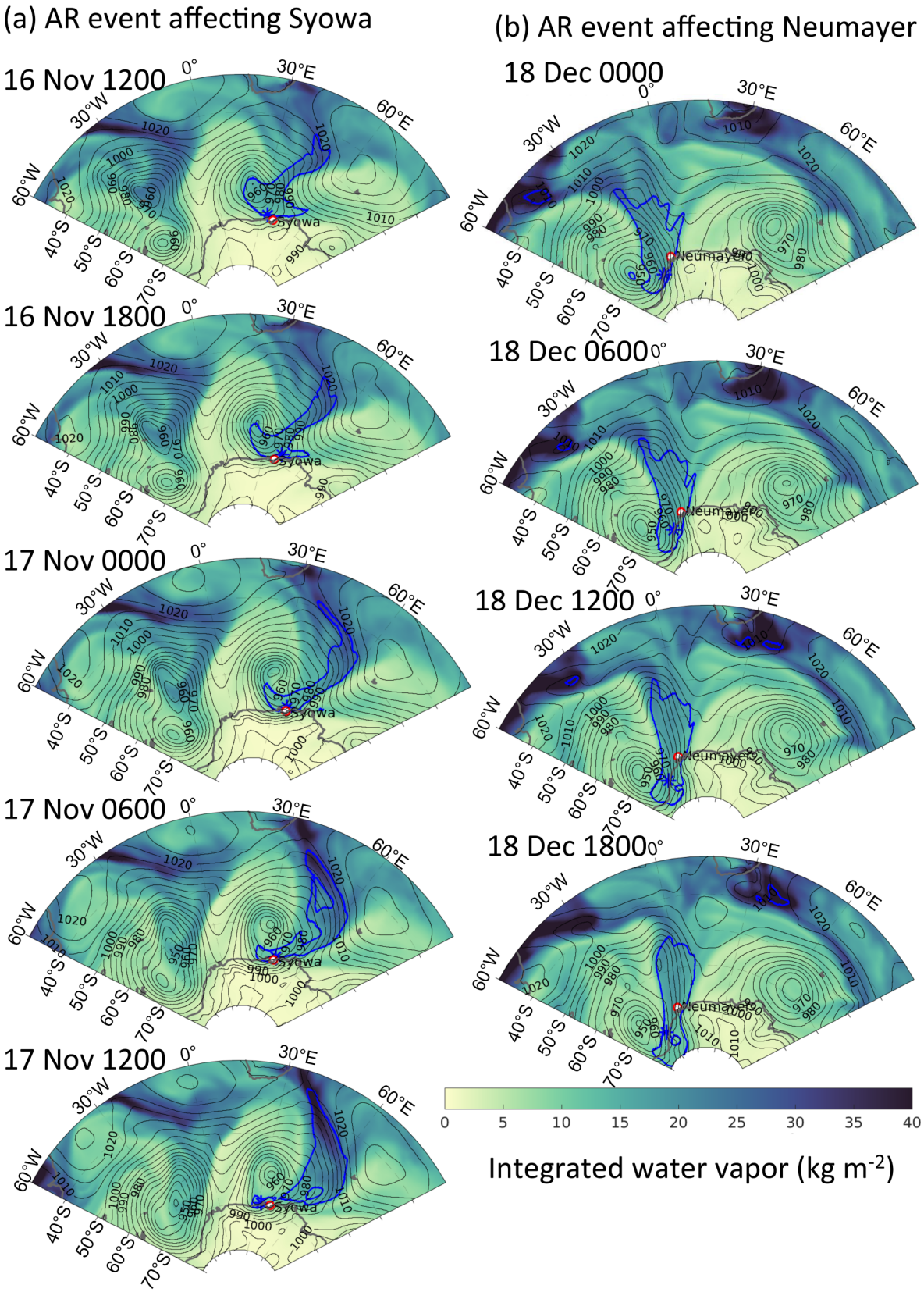

Fig. 2. Maps of IWV (colors; units: kg m^{-2}) and mean sea level pressure (contours; units: hPa) at each time step of the AR event with landfall (a) near Syowa station from 1200 UTC 16 November to 1200 UTC 17 November 2018, and (b) near Neumayer from 0000 UTC to 1800 UTC 18 December 2018. The fields are based on ERA-Interim reanalysis data. Blue contours show the AR boundaries defined using the AR algorithm (see section 3.2). Blue stars show the mean landfall location of the AR at the Antarctic coast. Red circles show the locations of Syowa and Neumayer stations.

regions. At the same time, the minimum IVT threshold of 100 kg m^{-1} s^{-1} used in the global algorithm by Guan and Waliser (2015) is a reasonable cut-off value for the two studied events.

The AR event affecting Syowa on 16–17 November 2018 was characterized by a corridor of moisture stretching from the western part of the Indian Ocean sector of the Southern Ocean (Fig. 2a). The AR contour shows an extent reaching far into the lower latitudes (as far as 38°S). While the mean longitude of the AR landfall was centered around 32°–43°E, the AR landfall spanned 166–950 km along the coast, depending on the time step (Table 1, Fig. 2a). The AR was associated with a deep low-pressure system centered at (60°S, 25°–30°E) and was blocked to the east by a pronounced high-pressure ridge.

During the AR event affecting Neumayer on 18 December 2018, a corridor with high IWV values was found stretching from the southern Atlantic Ocean (AR contour extending as far as 48°S) towards the eastern part of the Weddell Sea (Fig. 2b). The mean longitude of the AR landfall was centered at 20°–22°W, with the AR landfall spanning 850–1150 km along the coast (Table 1, Fig. 2b). As in the Syowa case in November, the AR affecting Neumayer in December was formed in association with a deep low-pressure system [centered in the northern Weddell Sea; (68°–70°S, ~40°E)], blocked by high pressure to the east.

A three-day backward trajectory analysis of the air parcels released at the locations of Neumayer and Syowa stations (at 500 m MSL) at the time of the AR landfall (figures not shown; see setup details in section 3.3) confirmed that the majority of the air parcels had a long-distance origin (south of 45°–50°S). This is consistent with the preferential direction of the two ARs extending into the subtropics (Fig. 2).

4.2. *AR signatures in radiosonde and reanalysis profiles*

The changes in the vertical profiles before, during and after the AR landfall in the vicinity of Neumayer and Syowa stations during the two prominent AR events are shown in Figs. 3 and 4.

4.2.1. *Neumayer*

The first time step of the AR landfalling near Neumayer on 18 December 2018 at 0000 UTC was characterized by increased total MT magnitude (see Appendix) in the extended layer between 950 and 750 hPa (up to 70 g kg^{-1} m s^{-1}) driven by relatively large specific humidity values [up to 3 g kg^{-1}, which is frequently attained in summer; see Fig. 5a and Lenaerts et al. (2010)] and strong wind speeds in the same layer (up to 30 m s^{-1}) veering from northeasterly near the ground to north-northeasterly above 800 hPa (Fig. 3a). The annual mean values for specific humidity and wind speed reported for Neumayer station are 1.2 g kg^{-1} and 9 m s^{-1} (van den Broeke et al., 2010). Near the ground (below 900 hPa), both zonal and meridional moisture flux components contributed to the total MT, while above 750 hPa the meridional (onshore) flux dominated (Fig. 3a). The observed profiles were well represented by both reanalyses (Fig. 3a, dashed and cross-dashed lines), with ERA5 showing a slightly stronger meridional MT component in the 900–850 hPa layer (Fig. 3a, right panel, red cross-dashed line). During this time at Neumayer, the IWV attained 12 kg m^{-2} and IVT 177 kg m^{-1} s^{-1} (according to radiosonde profiles), with IVT overestimated by both ERA-Interim and ERA5 (Table 1).

While the AR was persisting from 0000 to 1800 UTC on 18 December 2018 (Fig. 2b), the IWV and IVT at Neumayer reached their maximum values (15 kg m^{-2} and 340 kg m^{-1} s^{-1}) at 1800 UTC (Table 1, Fig. 3b). This peak IWV was well represented by both reanalyses, while IVT was slightly underestimated by ERA-Interim (330 kg m^{-1} s^{-1}) and well captured by ERA5 (343 kg m^{-1} s^{-1}) (Table 1). The peak IWV and IVT values at 1800 UTC are associated with an increase in the near-surface wind speed up to 32 m s^{-1}, with the maximum values at about 950 hPa and northeasterly in direction (Fig. 3b). This wind speed maximum is strongly underestimated by both reanalyses, which showed a maximum of only 22 m s^{-1} (Fig. 3b). As noted in section 2, easterly to northeasterly winds of high magnitude at Neumayer are typically associated with cyclonic disturbances and warm/moist advection, steered by the topography (Figs. 1a–c). The specific humidity profile was characterized by a strong inversion (up to 4 g kg^{-1}) between 900 and 850 hPa (above the LLJ) (Fig. 3b). At the same level, a temperature inversion can also be noted, indicating heat advection as it shows decoupling from the surface (Fig. 3b, left panel). The elevated humidity and temperature inversions are not well captured by ERA-Interim, while ERA5 represents the inversions quite closely, albeit slightly overestimating both temperature and humidity values near the surface (Figs. 3b). These moisture and temperature inversions can be explained by the enhanced onshore advection from the ocean, as it was found in the layers where the wind veers more towards the northerly direction (Fig. 3b). The wind direction in the moist layer is in the northeasterly quadrant, turning towards northerly with height, with the meridional (onshore) flux component dominating the total MT, attaining 100 g kg^{-1} m s^{-1} between 900 and 850 hPa (Fig. 3b). While the zonal MT component is well captured by both reanalyses, the meridional and the total MT are well captured only by ERA5, being underestimated by ERA-Interim (Fig. 3b).

After the AR's passing, high IVT values persisted at Neumayer until 1200 UTC 19 December (reaching 286 and 216 kg m^{-1} s^{-1} at 0600 UTC and 1200 UTC, respectively), with humidity inversion still present between 930 and 875 hPa and the near-surface LLJ weakening (Fig. 3c). Both reanalyses were still underestimating the LLJ and the peak in MT magnitude (Fig. 3c). During the entire AR event, the lower troposphere remained saturated, with RH_i showing a small oversaturation with respect to ice, being slightly underestimated by reanalyses (Figs. 3a–c). One day after the AR event (at 1800 UTC 19 December), a strong drying of the layers between 950 and 800 hPa occurred, while the temperature profile changed only slightly (Fig. 3d). This drying could be asso-

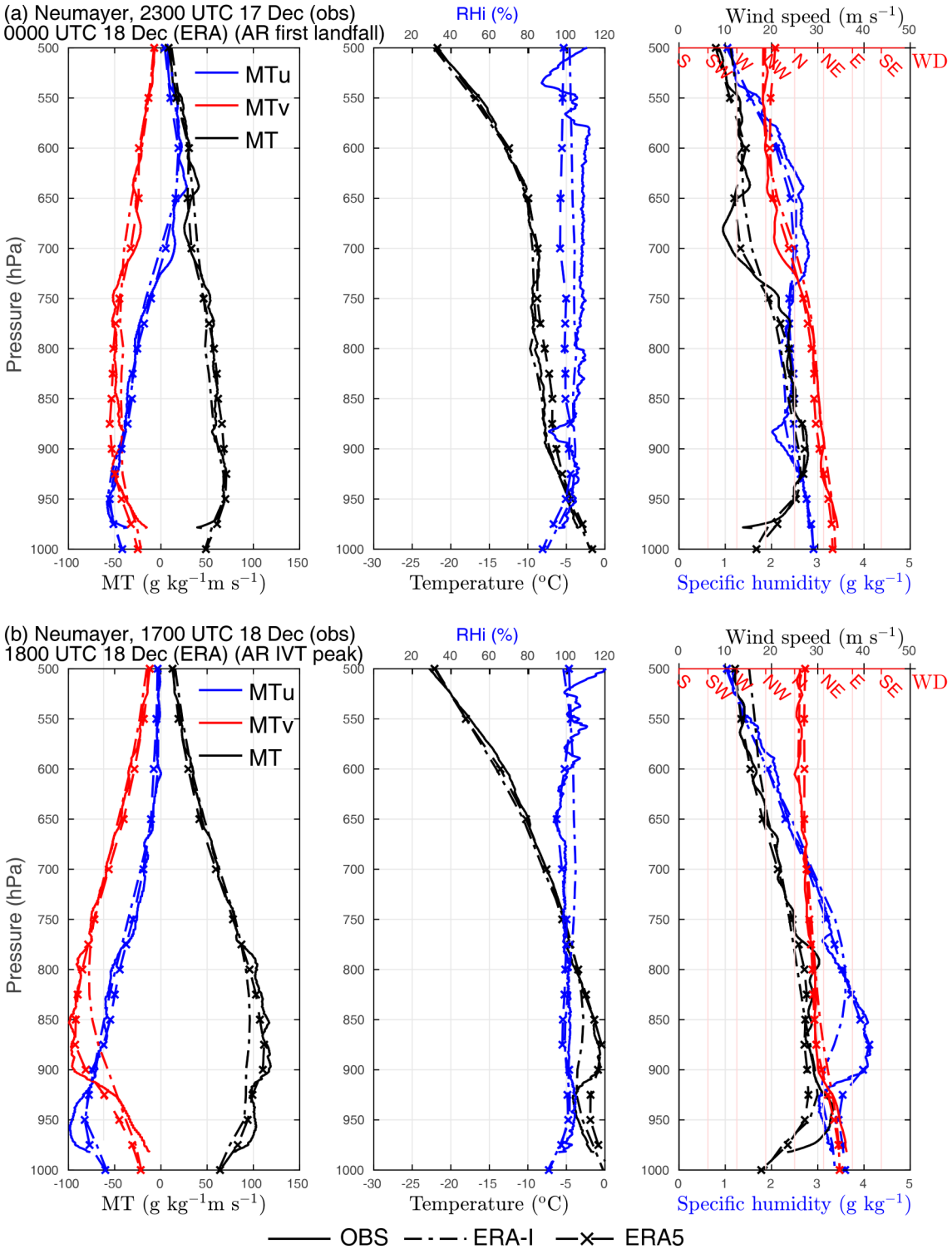

Fig. 3. Evolution of the vertical profiles (from 1000 to 500 hPa) at Neumayer's location during and after the AR event on 18 December 2018: zonal (MT_u, blue, positive eastward, negative westward) and meridional (MT_v, red, positive northward, negative southward) component vectors of moisture transport, and total moisture transport magnitude (MT, black) (left-hand panels); air temperature (black) and relative humidity with respect to ice (RH_i, blue) (center panels); specific humidity (blue), wind speed (black), and wind direction (red) (right-hand panels). Variables are derived from radiosonde measurements at Neumayer station (OBS, solid lines), and from ERA-Interim (ERA-I, dashed) and ERA5 (dashed with crosses) reanalysis data for the closest grid to the station. The radiosonde launch time (Obs) and the time step as in the reanalyses (ERA), together with the relevance to the AR event evolution, is indicated above each plot.

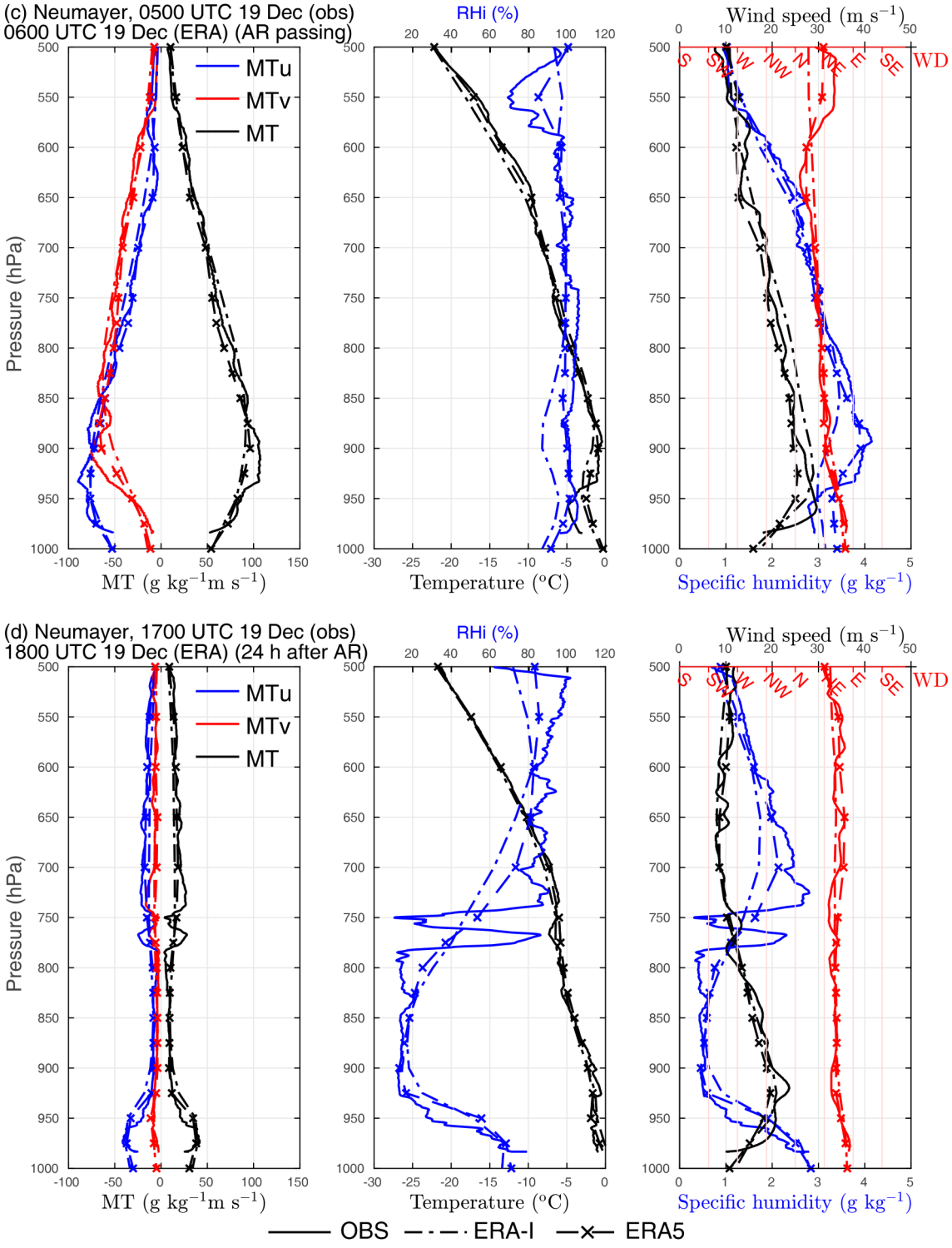

Fig. 3. (Continued).

ciated with the dry-air intrusion from near the tropopause frequently associated with the extratropical cyclone cold sector, as described by Browning (1997). MT suddenly dropped to below 50 g kg^{-1} m s^{-1} at 1800 UTC 19 December, with moisture inversion trapped near the surface and a dry layer present above 950 hPa (Fig. 3d). All these rapid changes were well captured by both reanalyses (Fig. 3d).

4.2.2. *Syowa*

During the AR event that affected Syowa on 16–17 November 2018, the enhanced MT was more influenced by a prominent LLJ between 900 and 825 hPa, while specific humidity attained maximum values near the surface (Figs. 4a and b). The IVT calculated using radiosonde measurements showed a maximum at 0000 UTC 17 November (192

kg m^{-1} s^{-1}; Table 1), when the total MT increased up to 100 g kg^{-1} m s^{-1} at about 920 hPa with equal contribution from zonal and meridional MT components (Fig. 4b), and coincident with the peak in the LLJ wind speed (Fig. 4b). Neither the increase in humidity near the surface nor the LLJ at higher levels were well captured by ERA-Interim and ERA5, both showing significant underestimation (Fig. 4b). This leads to significant underestimation of both the zonal and meridional MT components, and the total MT magnitude (Fig. 4b, left). The wind direction near the surface and in the lower troposphere had a persistent northeasterly direction throughout the AR event (Figs. 4a–c), indicating onshore advection from the ocean steered by the topography (and equally strong meridional and zonal MT compon-

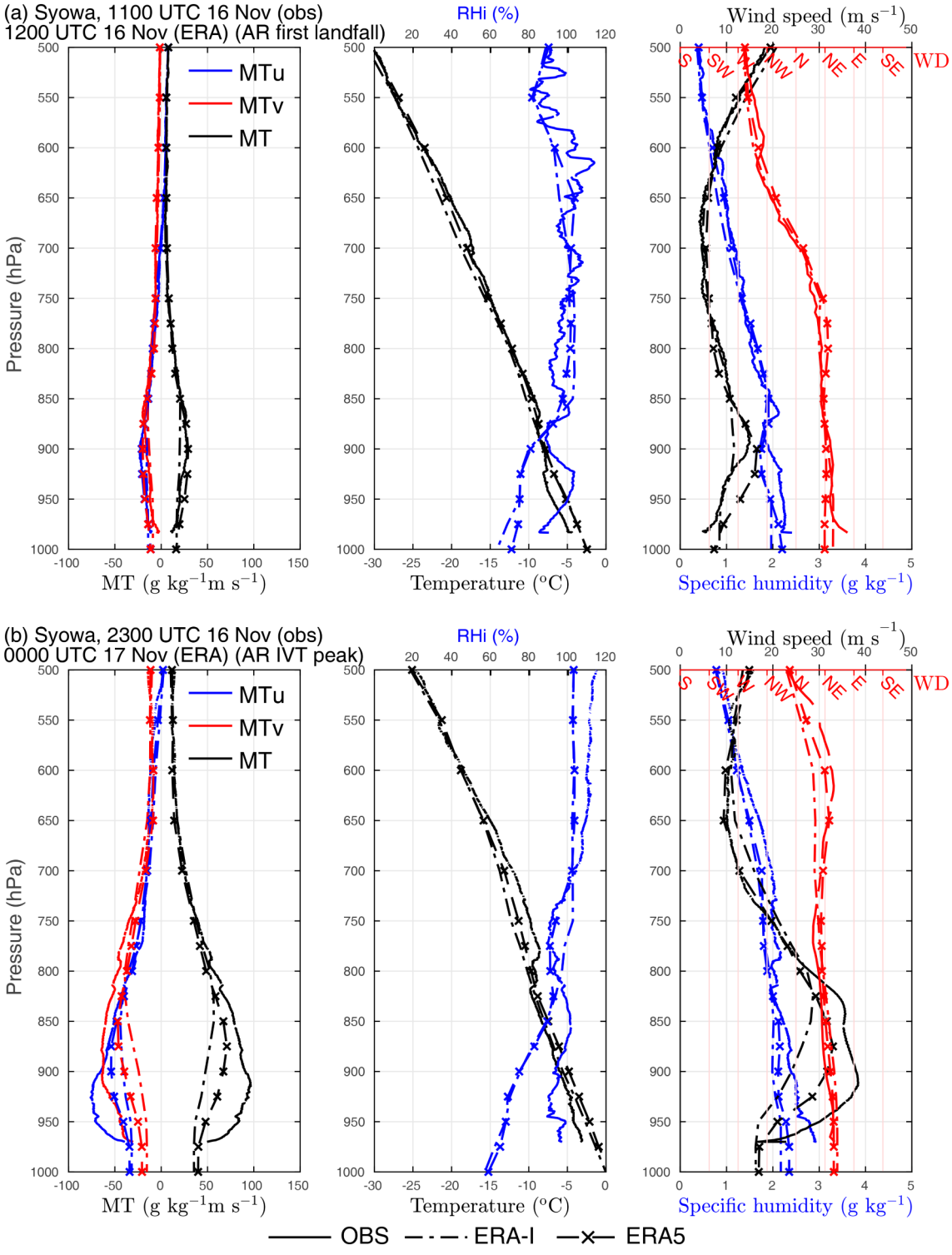

Fig. 4. As in Fig. 3 but for Syowa for the AR case on 16–17 November 2018.

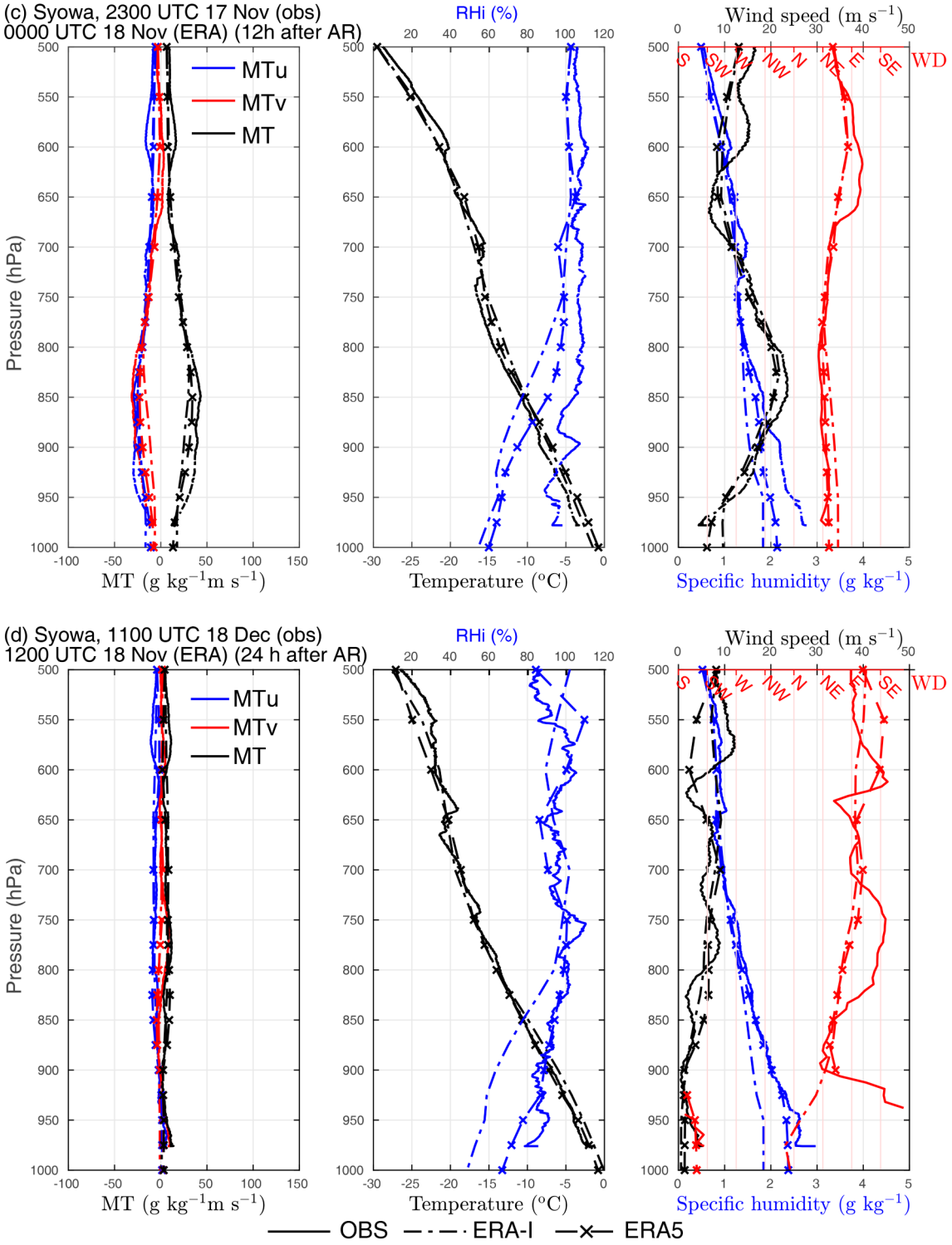

Fig. 4. (Continued).

ents; Fig. 4b). This lasted until a sudden change to the southerly wind direction below 900 hPa at 1200 UTC 18 November (Fig. 4d), typical of the katabatic flow from the plateau (see section 2 and Fig. 1d for wind regimes at Syowa). ERA-Interim and ERA5 show much stronger drying in the near-surface layers compared to radiosonde observations after the AR's passing (Figs. 4c and d). At the same time, as discussed in section 3.1.1, radiosondes are prone to wet bias in the dry layers situated above the humid layers. The wind direction shifting to the southerly direction is well captured by ERA5, while ERA-Interim instead shows a northerly direction (Fig. 4d).

4.3. *ARs and temporal evolution of vertical profiles*

Figures 5 and 6 demonstrate the temporal evolution of the vertical profiles of specific humidity, wind speed and

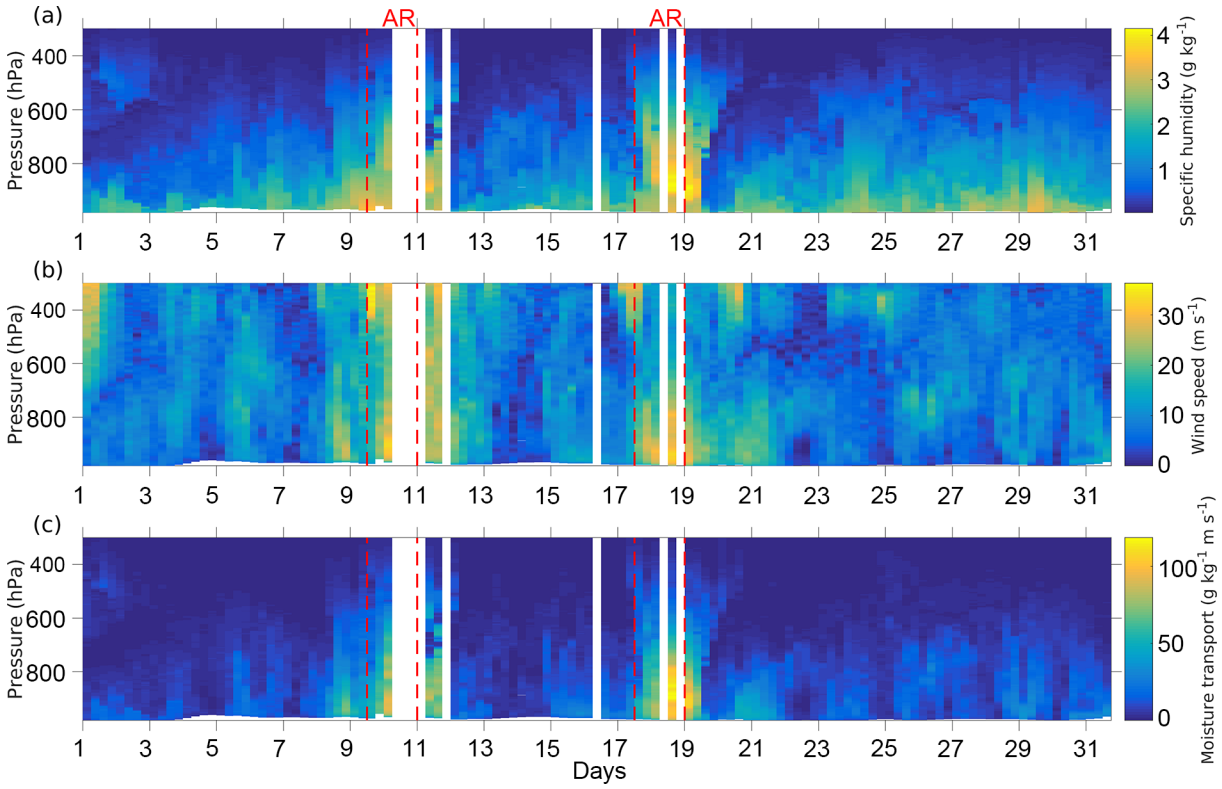

Fig. 5. Temporal evolution of the vertical profiles (from the first radiosonde measurement near the surface to 300 hPa) for (a) specific humidity, (b) wind speed, and (c) moisture transport during December 2018 at Neumayer, based on four radiosondes per day—at launch times of 0500, 1100, 1700, and 2300 UTC. Missing profiles are shown in white (see section 3.1.2 about data gaps). The red dashed lines show the periods when Neumayer experienced AR landfall.

MT at Syowa and Neumayer stations during November and December 2018, respectively, using frequent radiosonde observations during SOP-SH. AR events at Neumayer (indicated by red dashed lines in Fig. 5) show that the strong increase in specific humidity associated with ARs occupies a deep layer affecting almost the entire troposphere, with values peaking up to 4 g kg^{-1} between 800 and 925 hPa during at least one and a half days. At the same time, the wind speed increase is concentrated near the surface, with the LLJ directed along the topography in a northeasterly direction turning to northerly (onshore) when approaching 500 hPa (as shown by individual profiles in Fig. 3). The layers just above the surface are typically characterized by barrier jets (e.g., van den Broeke and Gallée, 1996) and katabatic flow (e.g., van den Broeke and van Lipzig, 2003), which many studies have found to be persistent and amplified during cyclonic disturbances and precipitation events (Parish, 1983; Parish and Bromwich, 2007; Seefeld and Cassano, 2008; van Wessem et al., 2015; Yamada and Hirasawa, 2018; Vignon et al., 2019). Enhanced easterly winds along the topography at the coastal and escarpments regions of DML are also associated with cyclonic disturbances and moisture influx from the lower latitudes, as opposed to the katabatic flow where the southerly component is present (König-Langlo and Loose, 2007; Gorodetskaya et al., 2013; Souverijns et al., 2018). The onshore moist advection occupies higher levels, with MT values much higher compared to the background state during the month (Fig. 5c), and compared to the median values as discussed in section 4.4 (Figs. 8 and 9).

The LLJ during the AR events is accompanied by a strong increase in the upper-level jet stream at the 300 hPa level (Fig. 5b), which can be an indication of a cyclonically induced LLJ when the low-level pressure decreases below the upper-level divergence in the left-hand exit region of a jet streak, which causes development of the ageostrophic component and horizontal acceleration, in turn causing the LLJ (e.g., Burrows et al., 2019). These LLJs assist in the poleward MT towards Antarctica during the ARs. The peak in the MT during the two AR cases affecting Neumayer station in December 2018 was found between 800 and 900 hPa, with significant values also below 900 hPa. Neumayer location on the ice shelf makes it sensitive to strong onshore MT not only at the peak level above 900 hPa, but also occurring closer to the surface—even if the flow follows the topography, it is initially associated with the moisture advection from the ocean.

The AR event at Syowa during 16–18 November 2018 also showed a strong and rapid change in the wind and humidity profiles compared to the rest of the month (Fig. 6). However, the AR signatures are different than those at Neumayer (Fig. 5). Firstly, both at Neumayer and Syowa stations there are elevated specific humidity values near the surface trapped in the stable boundary layer, with values up to

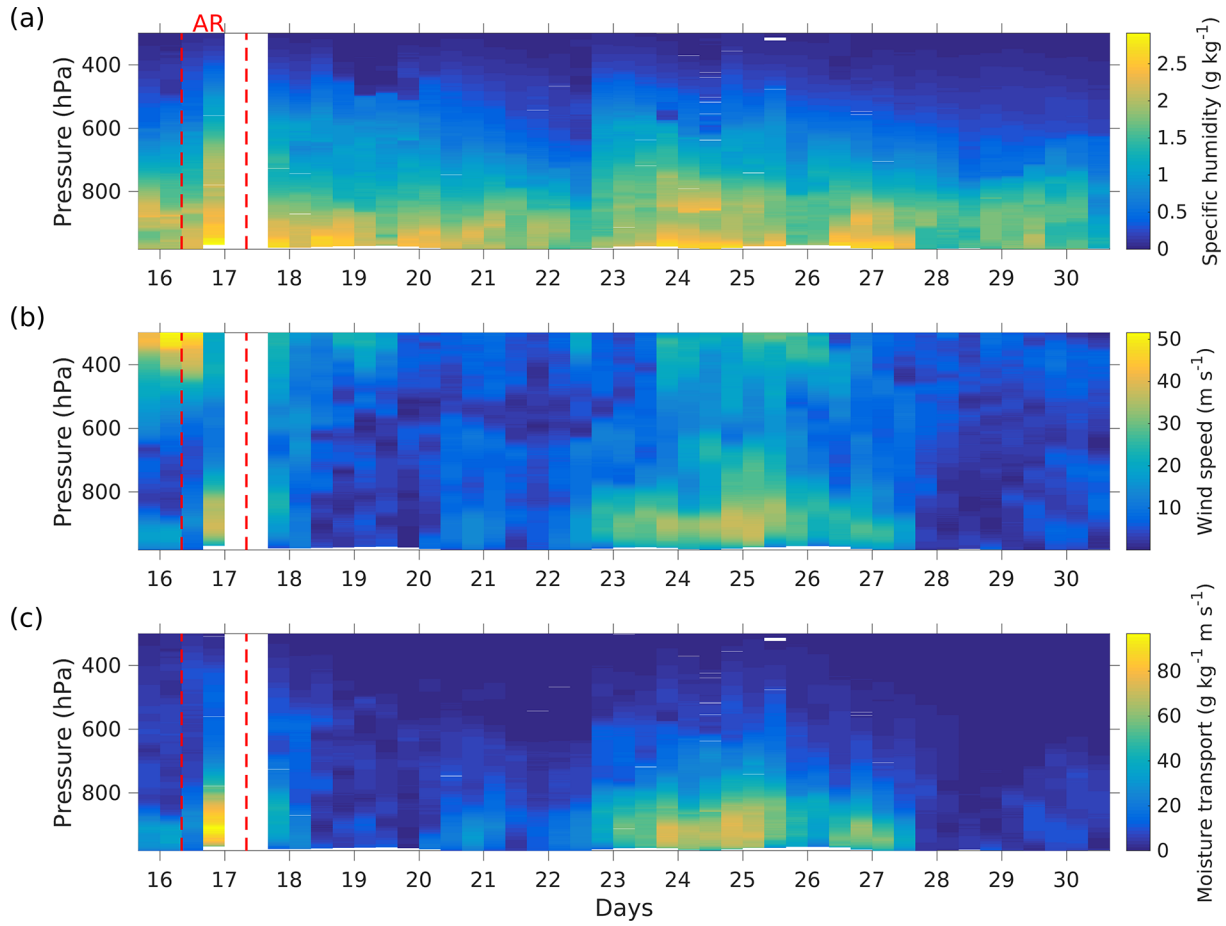

Fig. 6. As in Fig. 5 but for Syowa during 15–30 November 2018, based on three radiosondes per day—at launch times of 0500, 1100, and 2300 UTC. Missing profiles are shown in white (see section 3.1.2 about data gaps). The red dashed lines show the period when Syowa experienced AR landfall.

2–2.5 g kg^{-1}, during the entire months of November and December. At Neumayer, during the AR events, specific humidity values increased up to 4 g kg^{-1}, extending to higher levels, while at Syowa humidity values showed only a slight increase near the surface, with the height of the moist layer extending much less compared to Neumayer (Fig. 6a). At the same time, there was a much stronger increase in the wind speed below 900 hPa. This LLJ was accompanied by a very strong (up to 50 m s^{-1}) upper-level jet stream (Fig. 6b). The MT increase was not as strong compared to Neumayer, but still showed a significant anomaly up to 100 kg m^{-1} s^{-1} below 900 hPa (Fig. 6c).

4.4. *Enhanced MT events during 2009–19*

In order to put the AR events observed during YOPP SOP-SH into context over a longer period, we used radiosonde data at the two stations available via IGRA2 during a 10-yr period (2009–19). Analysis of the AR events detected during YOPP SOP-SH showed that they were all coincident with an enhanced MT signature in the vertical profiles, with IVT exceeding 100 kg m^{-1} s^{-1} and the maximum value in the MT profile exceeding 50 g kg^{-1} m s^{-1}. Distribution analysis applied to the maximum MT within the profile, and the IVT calculated based on IGRA2 radiosonde profiles, showed that these thresholds correspond to the 95th percentile based on the 2009–19 radiosonde measurements (Fig. 7).

Enhanced MT profiles were isolated according to the above mentioned criteria using IGRA2 radiosonde data during 2009–19 at Neumayer and Syowa. Figures 8 and 9 show the median and the interquartile range (from the 75th to 25th percentiles) for the composites of the enhanced MT profiles at both stations during the 10-yr period. It should be noted that these composites include the entire year of measurements, while YOPP SOP-SH was conducted during the austral summer period.

The composite profiles of the enhanced MT events at Neumayer show the peak values (median up to 58 g kg^{-1} m s^{-1} and 75th percentile up to 67 g kg^{-1} m s^{-1}) between 950 and 900 hPa (Fig. 8e). This peak is dominated by the zonal MT component (Fig. 8f), while the meridional MT component peaks at the higher levels between 900 and 850 hPa (Fig. 8g). Both ERA-Interim and ERA5 capture well the peak in total and zonal MT (Fig. 8e and f), with ERA-Interim showing smaller errors compared to ERA5 in total MT (Fig. 8l and m). Both reanalyses underestimate the peak in the meridional MT (Figs. 8g and n). The peak in the MT corresponds to the maximum wind speed within the same layer between 950 and 900 hPa, with median values up to 27 m s^{-1} and the

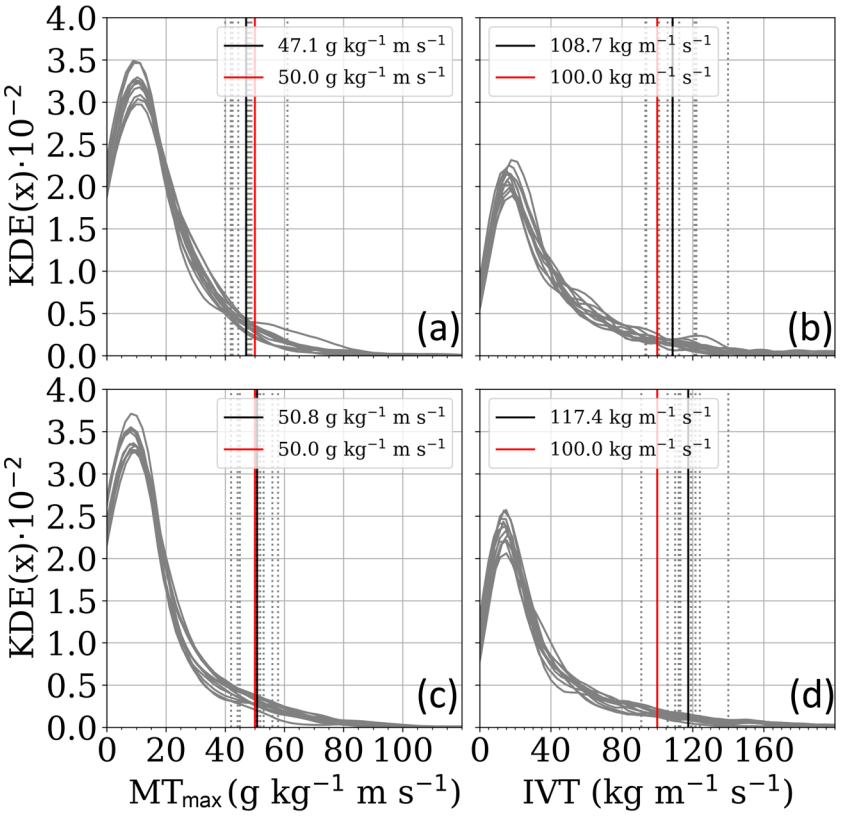

Fig. 7. Yearly distribution (as of kernel density estimation, KDE) of (a) maximum horizontal moisture transport (MT_{max}) and (b) integrated water vapor transport (IVT) within a profile related to enhanced moisture transport events at Neumayer. (c, d) As in (a, b) but for Syowa. Vertical dotted lines represent yearly 95th percentiles for the period 2009–19; the solid black line represents the median of all yearly 95th percentiles (value given in the legend); and the solid red line represents the applied thresholds (values in the legend).

75th percentile exceeding 32 m s^{-1} (Fig. 8c). Both reanalyses underestimate the median and the 75th percentile values of the wind peak (Figs. 8c and j). The location of the LLJ, its strength (up to 32 m s^{-1}), and the underestimation by both reanalyses are similar to the AR case on 18 December 2018 (Fig. 3b). At the same time, the composites do not show a pronounced elevated moisture inversion found during the December 2018 event (Fig. 8b and Fig. 3b), but rather show a small near-surface moisture inversion with median values up to 3 g kg^{-1} (Fig. 8b). This could be related to the low temporal resolution of regular radiosonde observations and reduced vertical resolution of IGRA2 archive data, which allows large-scale features to be captured whilst being unsuitable for analyzing small-scale changes in the tropospheric profile, including details of the humidity inversions and LLJs.

At Syowa, the composite of the enhanced MT events during 2009–19 (Fig. 9) shows similar signatures to the AR event observed during 16–17 November 2018 (Fig. 4). Firstly, the IGRA2 radiosonde-based composite shows a strong near-surface maximum in specific humidity, with the median peaking at 3.2 g kg^{-1} and 75th percentile up to 3.5 g kg^{-1} (Fig. 9b). This near-surface trapped humidity inversion is more pronounced compared to Neumayer (Fig. 8b). The near-surface humidity increase coincides with the warm layer, where the air temperature increase is up to 0°C (Fig. 9a), which is important in determining the precipitation phase and potential for surface melt. This finding is in line with earlier work by Kurita et al. (2016) showing that surface air temperature frequently exceeds 0°C during warm events at Syowa. This near-surface humidity inversion is completely missed by both reanalyses, underestimating the median value compared to the radiosonde composite by up to 0.7 g kg^{-1} (Fig. 9b, i).

A prominent increase in the wind speed is present in the composite median, with a peak between 925 and 875 hPa (Fig. 9c) and a persistent northeasterly direction throughout the lower troposphere (Fig. 9d). The intensity of this LLJ is strongly underestimated by the ERA-Interim composites, while ERA5 shows only a small underestimation (Fig. 9c, j). MT shows a moderate peak exceeding 60 g kg^{-1} m s^{-1} (with the 75th percentile reaching 50 g kg^{-1} m s^{-1}) within the heights of the wind speed maximum (Fig. 9e). The AR event affecting Syowa on 16–17 November 2018 showed an increase in MT up to 100 g kg^{-1} m s^{-1} (Fig. 4b), exceeding the 75th percentile of the 10-yr time series of enhanced

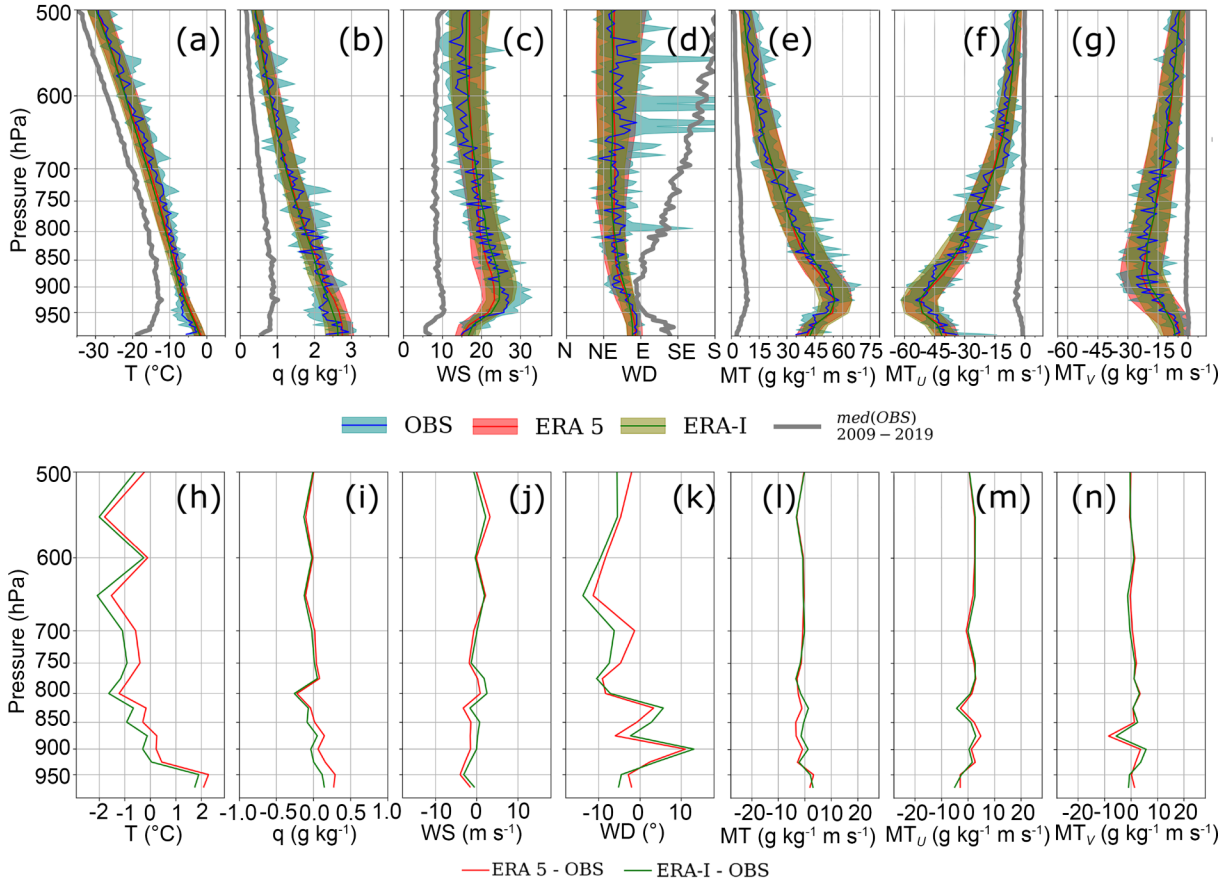

Fig. 8. Composite profiles from 1000 to 500 hPa (median and interquartile range) for all enhanced moisture transport events at Neumayer during 2009–19 for (a) temperature (T; units: °C), (b) specific humidity (q; units: g kg^{-1}), (c) wind speed (WS; units: m s^{-1}), (d) wind direction (WD—N = northerly, NE = northeasterly, E = easterly, SE = southeasterly), (e) moisture transport magnitude (MT; units: g kg^{-1} m s^{-1}), (f) MT zonal vector component (MT$_u$; units: g kg^{-1} m s^{-1}), (g) MT meridional vector component (MT$_v$; units: g kg^{-1} m s^{-1}). Variables are derived from radiosonde measurements at Neumayer station from the IGRA2 archive (OBS, cyan), from ERA-Interim (ERA-I, green) and ERA5 (red) for the closest grid to the station. The thick gray line on the composite profiles is the median based on the entire radiosonde period (2009–19). The radiosonde IGRA2 original profiles are interpolated to 5-hPa intervals from the first layer near the surface to 500 hPa. Differences between the reanalyses and observations (for ERA-Interim in green, for ERA5 in red) for respective variables are given in panels (h–n).

MT events. The total MT and its both components are strongly underestimated by both reanalyses, with ERA5 showing a smaller but still strong bias (Figs. 9e–g, and l–n).

5. Conclusions and outlook

ARs make an important contribution to the MT towards the Antarctic ice sheet by linking moisture sources in lower latitudes to the Antarctic surface mass balance. Here, we analyze AR signatures in the atmospheric vertical profiles at the sites of Neumayer and Syowa, located in the coastal region of DML, East Antarctica. Our study is based on extra radiosonde measurements conducted during YOPP SOP-SH from 15 November 2018 to 15 February 2019. Further, regular radiosonde measurements (using the IGRA2 archive) are used to construct enhanced MT composites during 2009–19. Both individual AR event profiles and the 10-yr composites are compared to ERA-Interim and ERA5 reanalysis products. Detailed analysis of two prominent AR events affecting the locations of Neumayer and Syowa, possible due to the more frequent radiosonde observations during YOPP SOP-SH, showed a significant increase in specific humidity extending through the mid-troposphere and the presence of a strong LLJ. At Neumayer, the peak in the moisture inversion was found between 800 and 900 hPa, while the LLJ was concentrated below 900 hPa. At Syowa, the increase in humidity was concentrated near the surface, while enhanced MT was mostly driven by a substantial increase in the wind speed (up to 40 m s^{-1}) between 825 and 925 hPa. MT during the ARs identified during YOPP in austral summer always exceeded 50 g kg^{-1} m s^{-1} and occasionally was greater than 100 g kg^{-1} m s^{-1}, always with a strong meridional component indicating onshore MT. IVT reached a maximum of 200 kg m^{-1} s^{-1} at Syowa and 340 kg m^{-1} s^{-1} at Neumayer. When compared to the individual events analyzed during YOPP SOP-SH using high vertical resolution radiosonde data, ERA5 shows significant improvement compared to ERA-Interim for Neumayer profiles representing

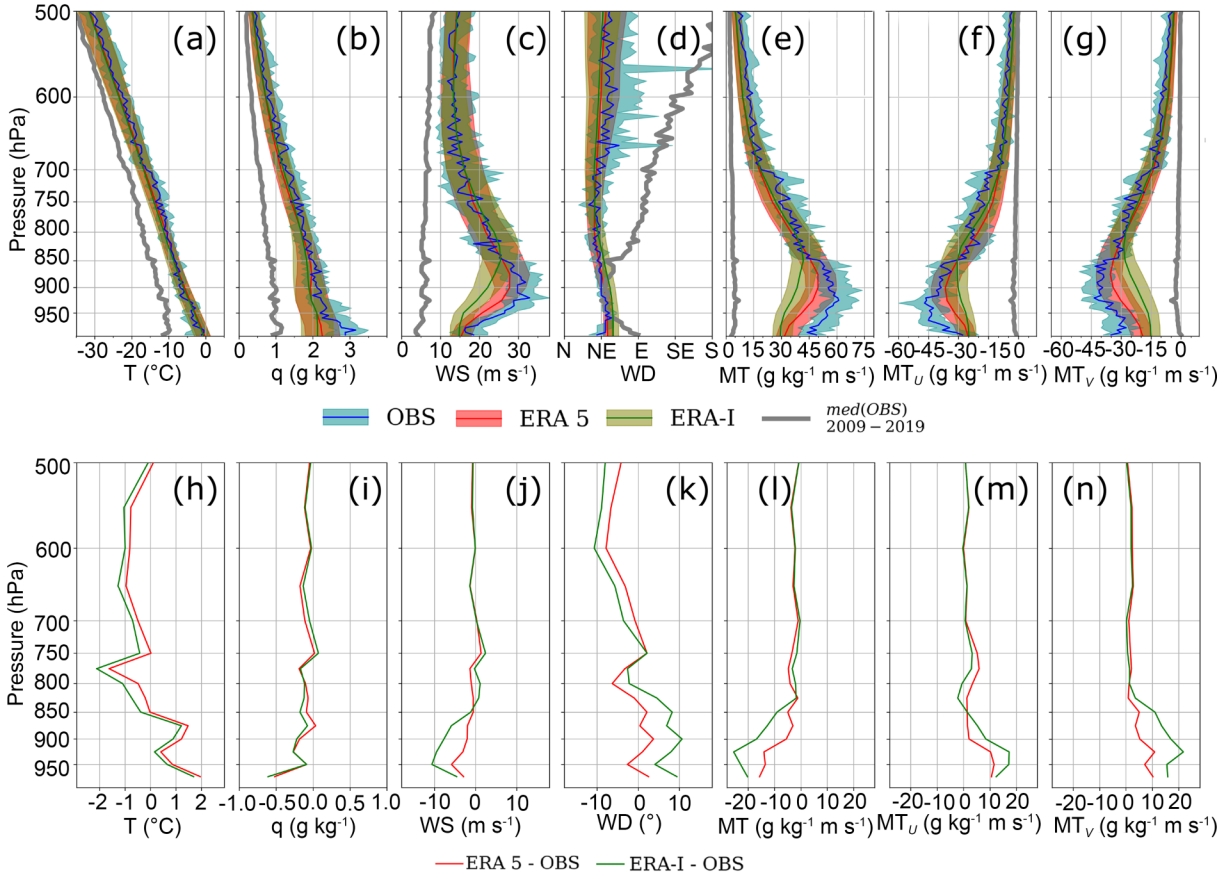

Fig. 9. As in Fig. 8 but for Syowa station.

the AR peak values, while underestimating the LLJ magnitude and humidity inversion near the surface for Syowa, leading to the underestimation of MT.

Composites of the enhanced MT events at both stations during a 10-yr period (January 2009 to October 2019) show that these events represent an extreme state of the lower-tropospheric profile compared to its median values with respect to all variables (temperature, humidity, wind speed and, consequently, MT magnitude). Large-scale features of the enhanced MT events composites are relatively well represented by both ERA-Interim and ERA5.

The individual AR events during the YOPP SOP-SH period and the composite analysis of enhanced MT events during 2009–19 show significantly larger values of moisture flux into the Antarctic ice sheet at its boundary compared to the median atmospheric profile values and mean monthly estimates demonstrated in earlier studies (Dufour et al., 2019). We have shown that the enhanced MT during ARs is linked to a strong increase in specific humidity and wind speed, with a significant meridional (onshore) component within the 950–800 hPa layer on short time scales (several hours to 1–2 days). Analysis of such events requires high spatial, vertical and temporal resolution reanalysis/model products and observations. The increased frequency of radiosonde observations during YOPP SOP-SH allowed the present analysis of AR events and their contribution to the MT towards Antarctica. However, measurements during these events were frequently missed even by those stations with regular radiosonde observations, due to severe weather conditions precluding operations at the station. This points to a possible bias in the available radiosonde observations in terms of missing the most significant events, which can influence climatological and long-time-series analyses. Recent state-of-the-art reanalysis products, which can fill these gaps, capture relatively well the large-scale features of these events, but miss the large peaks in humidity and wind speeds, and thus the exact magnitude and height of the enhanced MT. Improvements in AR representation in models can be made via further evaluation and process-oriented studies using targeted measurement campaigns.

APPENDIX

Calculation of Variables

Both Neumayer and Syowa stations report dewpoint temperature (T_d) near the surface, which is converted to vapor pressure (e) (section 2; Figs. 1c and e) using the Magnus Tetens equation (Murray, 1967) for vapor pressure over liquid water below 0°C:

$$e = 6.1078 \exp\left[\frac{17.2693882(T_d - 273.16)}{T_d - 35.86}\right], \qquad \text{(A1)}$$

where T_d is in units of K and e is in units of hPa.

Standard capacitive humidity sensors used in radiosondes measure RH over liquid water, even at subfreezing temperatures. Specific humidity (q, kg kg^{-1}) profiles are thus calculated as follows:

$$e_s = 6.112 \exp\left(\frac{17.67T}{243.5+T}\right), \quad \text{(A2)}$$

$$q \cong w = \frac{\mathrm{RH}}{100}\varepsilon\frac{e_s}{p-e_s}, \quad \text{(A3)}$$

where e_s (units: hPa) is the saturated vapor pressure over liquid water below 0°C calculated using the equation from Bolton (1980), T is air temperature (units: °C), w is the water vapor mixing ratio (units: kg kg^{-1}), RH is in %, $\varepsilon = M_v/M_d = 0.622$, and p is air pressure (units: hPa). The equations from Murray (1967) and Bolton (1980) give very close results for e_s. As noted by Bolton (1980), Eq. (A2) fits experimental data results down to −35°C. RH with respect to ice ($\mathrm{RH_i}$) is calculated as $\mathrm{RH_i} = \mathrm{RH}(e_s/e_{si})$, where e_{si} is saturated vapor pressure over ice calculated using coefficients adjusted for ice (Murray, 1967).

In order to compute saturated IWV ($\mathrm{IWV_{sat}}$) for the AR algorithm (section 3.2), saturated vapor pressure is calculated based on T profiles from ERA-Interim. For $T < 0$°C, water vapor can be saturated in equilibrium with liquid or ice, and here saturation vapor pressure over water is used to calculate a theoretical maximum value of $\mathrm{IWV_{sat}}$. Our analysis shows that, during AR events, the troposphere can be saturated or close to saturation over water from the surface up to at least 500 hPa, reaching supersaturation with respect to ice at some levels (Figs. 3 and 4).

Integrated water vapor (kg m^{-2}):

$$\mathrm{IWV} = -\frac{1}{g}\int_{P_s}^{P_t} q\,\mathrm{d}p, \quad \text{(A4)}$$

where g is gravitational acceleration (= 9.81 m s^{-2}), p is pressure (units: Pa), P_s is the first pressure level near the surface, and P_t = 300 hPa.

Saturated IWV (units: kg m^{-2}):

$$\mathrm{IWV_{sat}} = -\frac{1}{g}\int_{P_s}^{P_t} q_s(T)\,\mathrm{d}p, \quad \text{(A5)}$$

where q_s is saturated specific humidity calculated based on e_s [Eq. (A2)].

Zonal moisture transport (MT) vector component (MT_u; units: kg kg^{-1} m s^{-1}):

$$\mathrm{MT}_u = qu, \quad \text{(A6)}$$

where u is the zonal wind vector component (units: m s^{-1}).

Meridional MT vector component (MT_v; units: kg kg^{-1} m s^{-1}):

$$\mathrm{MT}_v = qv, \quad \text{(A7)}$$

where v is the meridional wind vector component (units: m s^{-1}).

Total MT magnitude (units: kg kg^{-1} m s^{-1}):

$$\mathrm{MT} = q\sqrt{u^2+v^2} = q\mathrm{WS}, \quad \text{(A8)}$$

where WS is wind speed (units: m s^{-1}).

Integrated Vapor (Moisture) Transport (units: kg m^{-1} s^{-1}):

$$\mathrm{IVT} = \sqrt{\left(\frac{1}{g}\int_{P_t}^{P_s}\mathrm{MT}_u\mathrm{d}p\right)^2 + \left(\frac{1}{g}\int_{P_t}^{P_s}\mathrm{MT}_v\mathrm{d}p\right)^2}. \quad \text{(A9)}$$

Data Availability

The radiosonde data conducted during YOPP SOP-SH are publicly available via the British Antarctic Survey depository (ftp://ftp.bas.ac.uk/src/YOPP-SH/radiosondes/) (contact person: Steve COLWELL). IGRA data are publicly available via the NOAA National Centers for Environmental Information (https://www.ncdc.noaa.gov/data-access/weather-balloon/integrated-global-radiosonde-archive). ERA-Interim and ERA5 fields are available via the ECMWF and Copernicus Climate Change Service Climate Data Store (https://www.ecmwf.int/). The AR algorithm used in the study is part of the Atmospheric River Tracking Method Intercomparison Project (ARTMIP, http://www.cgd.ucar.edu/projects/artmip/).

Acknowledgements. This is a contribution to the Year of Polar Prediction (YOPP), a flagship activity of the Polar Prediction Project (PPP) initiated by the World Weather Research Programme (WWRP) of the World Meteorological Organisation (WMO). We acknowledge the WMO WWRP for its role in coordinating this international research activity. We thank personnel and National Antarctic programs of Germany and Japan carrying out meteorological measurements at Neumayer and Syowa stations. We thank Steve COLWELL for providing the Antarctic YOPP radiosonde data archive. Special thanks to Kirstin WERNER, director of the International Coordination Office for Polar Prediction, Alfred WEGENER Institute, for her continuous support regarding YOPP activities. The authors gratefully acknowledge the NOAA Air Resources Laboratory (ARL) for the provision of the HYSPLIT transport and dispersion model and READY website (http://www.ready.noaa.gov) used in this publication. I.V.G. thanks FCT/MCTES for the financial support to CESAM (UID/AMB/50017/2019) through national funds and FCT grant CIRCNA/CAC/0273/2019. NH thanks National Institute of Polar Research (NIPR) Project Research No. KP302. The authors are grateful to the journal editorial team and two anonymous reviewers for their useful and constructive comments and suggestions.

REFERENCES

Bintanja, R., 2000: Snowdrift suspension and atmospheric turbulence. Part I: Theoretical background and model description. *Bound.-Layer Meteorol.*, **95**, 343–368, https://doi.org/10.1023/A:1002676804487.

Boening, C., M. Lebsock, F. Landerer, and G. Stephens, 2012: Snowfall-driven mass change on the East Antarctic ice sheet. *Geophys. Res. Lett.*, **39**, L21501, https://doi.org/10.1029/2012GL053316.

Bolton, D., 1980: The computation of equivalent potential temperature. *Mon. Wea. Rev.*, **108**, 1046–1053, https://doi.org/10.1175/1520-0493(1980)108<1046:TCOEPT>2.0.CO;2.

Bozkurt, D., R. Rondanelli, J. C. Marín, and R. Garreaud, 2018: Foehn event triggered by an atmospheric river underlies record-setting temperature along continental Antarctica. *J. Geophys. Res.*, **123**, 3871–3892, https://doi.org/10.1002/2017JD027796.

Bromwich, D. H., F. M. Robasky, R. I. Cullather, and M. L. van Woert, 1995: The atmospheric hydrologic cycle over the Southern Ocean and Antarctica from operational numerical analyses. *Mon. Wea. Rev.*, **123**, 3518–3538, https://doi.org/10.1175/1520-0493(1995)123<3518:TAHCOT>2.0.CO;2.

Browning, K. A., 1997: The dry intrusion perspective of extra-tropical cyclone development. *Meteorological Applications*, **4**, 317–324, https://doi.org/10.1017/S1350482797000613.

Burrows, D. A., C.R. Ferguson, M.A. Campbell, G. Xia, and L.F. Bosart, 2019: An Objective Classification and Analysis of Upper-Level Coupling to the Great Plains Low-Level Jet over the Twentieth Century. *J. Climate*, **32**, 7127–7152, https://doi.org/10.1175/JCLI-D-18-0891.1.

Connolley, W. M., and J. C. King, 1993: Atmospheric water-vapour transport to Antarctica inferred from radiosonde data. *Quart. J. Roy. Meteorol. Soc.*, **119**, 325–342, https://doi.org/10.1002/qj.49711951006.

Cordeira, J. M., F. M. Ralph, A. Martin, N. Gaggini, J. R. Spackman, P. J. Neiman, J. J. Rutz, and R. Pierce, 2017: Forecasting atmospheric rivers during CalWater 2015. *Bull. Amer. Meteorol. Soc.*, **98**, 449–459, https://doi.org/10.1175/BAMS-D-15-00245.1.

Dee, D. P., and Coauthors, 2011: The ERA-Interim reanalysis: Configuration and performance of the data assimilation system. *Quart. J. Roy. Meteorol. Soc.*, **137**, 553–597, https://doi.org/10.1002/qj.828.

Dufour, A., C. Charrondière, and O. Zolina, 2019: Moisture transport in observations and reanalyses as a proxy for snow accumulation in East Antarctica. *The Cryosphere*, **13**, 413–425, https://doi.org/10.5194/tc-13-413-2019.

Durre, I., and X. G. Yin, 2008: Enhanced radiosonde data for studies of vertical structure. *Bull. Amer. Meteorol. Soc.*, **89**, 1257–1262, https://doi.org/10.1175/2008BAMS2603.1.

Durre, I., R. S. Vose, and D. B. Wuertz, 2008: Robust automated quality assurance of radiosonde temperatures. *Journal of Applied Meteorology & Climatology*, **47**, 2081–2095, https://doi.org/10.1175/2008JAMC1809.1.

Durre, I., X. G. Yin, R. S. Vose, S. Applequist, and J. Arnfield, 2016: Integrated Global Radiosonde Archive (IGRA) Version 2. [Sounding data for the full period of record]. NOAA National Centers for Environmental Information, https://doi.org/10.7289/v5x63k0q.

Ferreira, A. P., R. Nieto, and L. Gimeno, 2019: Completeness of radiosonde humidity observations based on the Integrated Global Radiosonde Archive. *Earth System Science Data*, **11**, 603–627, https://doi.org/10.5194/essd-11-603-2019.

Fretwell, P., and Coauthors, 2013: Bedmap2: Improved ice bed, surface and thickness datasets for Antarctica. *The Cryosphere*, **7**, 375–393, https://doi.org/10.5194/tc-7-375-2013.

Gettelman, A., V. P. Walden, L. M. Miloshevich, W. L. Roth, and B. Halter, 2006: Relative humidity over Antarctica from radiosondes, satellites, and a general circulation model. *J. Geophys. Res.*, **111**, D09S13, https://doi.org/10.1029/2005JD006636.

Gorodetskaya, I. V., N. P. M. van Lipzig, M. R. van den Broeke, A. Mangold, W. Boot, and C. H. Reijmer, 2013: Meteorological regimes and accumulation patterns at Utsteinen, Dronning Maud Land, East Antarctica: Analysis of two contrasting years. *J. Geophys. Res.*, **118**, 1700–1715, https://doi.org/10.1002/jgrd.50177.

Gorodetskaya, I. V., M. Tsukernik, K. Claes, M. F. Ralph, W. D. Neff, and N. P. M. van Lipzig, 2014: The role of atmospheric rivers in anomalous snow accumulation in East Antarctica. *Geophys. Res. Lett.*, **41**, 6199–6206, https://doi.org/10.1002/2014GL060881.

Gossart, A., and Coauthors, 2017: Blowing snow detection from ground-based ceilometers: Application to East Antarctica. *The Cryosphere*, **11**, 2755–2772, https://doi.org/10.5194/tc-11-2755-2017.

Guan, B., and D. E. Waliser, 2015: Detection of atmospheric rivers: Evaluation and application of an algorithm for global studies. *J. Geophys. Res.*, **120**, 12 514–12 535, https://doi.org/10.1002/2015JD024257.

Hersbach, H., and Coauthors, 2019: Global reanalysis: Goodbye ERA-Interim, hello ERA5. ECMWF Newsletter No. 159, https://doi.org/10.21957/vf291hehd7.

Hirasawa, N., 2017: Japanese activity and plan for YOPP-SH. YOPP-SH Workshop, National Center for Atmospheric Research, Boulder, Colorado, USA, 28 June 2017–29 June 2017. [Available online from http://polarmet.osu.edu/YOPP-SH/Presentations_201706/1_03_Hirasawa.pdf]

Ingleby, B., 2017: An assessment of different radiosonde types 2015/2016. ECMWF Technical Memoranda 807, https://doi.org/10.21957/0nje0wpsa.

Jakobs, C. L., C. H. Reijmer, P. Kuipers Munneke, G. König-Langlo, and M. R. van den Broeke, 2019: Quantifying the snowmelt-albedo feedback at Neumayer Station, East Antarctica. *The Cryosphere*, **13**, 1473–1485, https://doi.org/10.5194/tc-13-1473-2019.

Jensen, M. P., D. J. Holdridge, P. Survo, R. Lehtinen, S. Baxter, T. Toto, and K. L. Johnson, 2016: Comparison of Vaisala radiosondes RS41 and RS92 at the ARM southern Great Plains site. *Atmospheric Measurement Techniques*, **9**, 3115–3129, https://doi.org/10.5194/amt-9-3115-2016.

Jung, T., and Coauthors, 2016: Advancing polar prediction capabilities on daily to seasonal time scales. *Bull. Amer. Meteorol. Soc.*, **97**, 1631–1647, https://doi.org/10.1175/BAMS-D-14-00246.1.

Kawai, Y., M. Katsumata, K. Oshima, M. E. Hori, and J. Inoue, 2017: Comparison of Vaisala radiosondes RS41 and RS92 launched over the oceans from the Arctic to the tropics. *Atmospheric Measurement Techniques*, **10**, 2485–2498, https://doi.org/10.5194/amt-10-2485-2017.

King, M. A., R. J. Bingham, P. Moore, P. L. Whitehouse, M. J. Bentley, and G. A. Milne, 2012: Lower satellite-gravimetry estimates of Antarctic sea-level contribution. *Nature*, **491**,

586–589, https://doi.org/10.1038/nature11621.

Kizu, N., T. Sugidachi, E. Kobayashi, S. Hoshino, K. Shimizu, R. Maeda, and M. Fujiwara, 2018: Technical characteristics and GRUAN data processing for the Meisei RS-11G and iMS-100 radiosondes. GRUAN-TD-5). GRUAN Lead Centre, Lindenberg, Germany.

Klöwer, M., T. Jung, G. König-Langlo, and T. Semmler, 2013: Aspects of weather parameters at Neumayer station, Antarctica, and their representation in reanalysis and climate model data. *Meteorol. Z.*, **22**, 699–709, https://doi.org/10.1127/0941-2948/2013/0505.

Knippertz, P., H. Wernli, and G. Gläser, 2013: A global climatology of tropical moisture exports. *J. Climate*, **26**, 3031–3045, https://doi.org/10.1175/JCLI-D-12-00401.1.

Kobayashi, E., S. Hoshino, M. Iwabuchi, T. Sugidachi, K. Shimizu, and M. Fujiwara, 2019: Comparison of the GRUAN data products for Meisei RS-11G and Vaisala RS92-SGP radiosondes at Tateno (36.06°N, 140.13°E), Japan. *Atmospheric Measurement Techniques*, **12**, 3039–3065, https://doi.org/10.5194/amt-12-3039-2019.

König-Langlo, G., and B. Loose, 2007: The meteorological observatory at Neumayer stations (GvN and NM-II) Antarctica. *Polarforschung*, **76**, 25–38.

König-Langlo, G., J. C. King, and P. Pettré, 1998: Climatology of the three coastal Antarctic stations Dumont D'urville, Neumayer, and Halley. *J. Geophys. Res.*, **103**, 10 935–10 946, https://doi.org/10.1029/97JD00527.

Konishi, H., M. Wada, and T. Endoh, 1998: Seasonal variations of cloud and precipitation at Syowa Station, Antarctica. *Annals of Glaciology*, **27**, 597–602, https://doi.org/10.3189/1998AoG27-1-597-602.

Kurita, N., N. Hirasawa, S. Koga, J. Matsushita, H. C. Steen-Larsen, V. Masson-Delmotte, and Y. Fujiyoshi, 2016: Identification of air masses responsible for warm events on the East Antarctic Coast. *SOLA*, **12**, 307–313, https://doi.org/10.2151/sola.2016-060.

Lenaerts, J. T. M., M. R. van den Broeke, S. J. Déry, G. König-Langlo, J. Ettema, and P. K. Munneke, 2010: Modelling snowdrift sublimation on an Antarctic ice shelf. *The Cryosphere*, **4**, 179–190, https://doi.org/10.5194/tc-4-179-2010.

Lenaerts, J. T. M., E. van Meijgaard, M. R. van den Broeke, S. R. M. Ligtenberg, M. Horwath, and E. Isaksson, 2013: Recent snowfall anomalies in Dronning Maud Land, East Antarctica, in a historical and future climate perspective. *Geophys. Res. Lett.*, **40**, 2684–2688, https://doi.org/10.1002/grl.50559.

Murray, F. W., 1967: On the computation of saturation vapor pressure. *J. Appl. Meteor*, **6**, 203–204, https://doi.org/10.1175/1520-0450(1967)006<0203:OTCOSV>2.0.CO;2.

Nash, D., D. Waliser, B. Guan, B., H. C. Ye, and F. M. Ralph, 2018: The role of atmospheric rivers in extratropical and polar hydroclimate. *J. Geophys. Res.*, **123**, 6804–6821, https://doi.org/10.1029/2017JD028130.

Nygård, T., T. Valkonen, and T. Vihma, 2013: Antarctic low-tropospheric humidity inversions: 10-yr climatology. *J. Climate*, **26**, 5205–5219, https://doi.org/10.1175/JCLI-D-12-00446.1.

Parish, T. R., 1983: The influence of the Antarctic Peninsula on the wind field over the western Weddell Sea. *J. Geophys. Res.*, **88**, 2684–2692, https://doi.org/10.1029/JC088iC04p02684.

Parish, T. R., and D. H. Bromwich, 2007: Reexamination of the near-surface airflow over the Antarctic continent and implications on atmospheric circulations at high southern latitudes. *Mon. Wea. Rev.*, **135**, 1961–1973, https://doi.org/10.1175/MWR3374.1.

Ralph, F. M., P. J. Neiman, and G. A. Wick, 2004: Satellite and CALJET aircraft observations of atmospheric rivers over the eastern North Pacific Ocean during the winter of 1997/98. *Mon. Wea. Rev.*, **132**, 1721–1745, https://doi.org/10.1175/1520-0493(2004)132<1721:SACAOO>2.0.CO;2.

Ralph, F. M., J. M. Cordeira, P. J. Neiman, and M. Hughes, 2016: Landfalling Atmospheric Rivers, the Sierra Barrier Jet, and extreme daily precipitation in northern California's Upper Sacramento River Watershed. *Journal of Hydrometeorology*, **17**, 1905–1914, https://doi.org/10.1175/JHM-D-15-0167.1.

Ralph, F. M., J. J. Rutz, J. M. Cordeira, M. Dettinger, M. Anderson, D. Reynolds, L. J. Schick, and C. Smallcomb, 2019: A scale to characterize the strength and impacts of atmospheric rivers. *Bull. Amer. Meteorol. Soc.*, **100**, 269–289, https://doi.org/10.1175/BAMS-D-18-0023.1.

Rowe, P. M, L. M. Miloshevich, D. D. Turner, and V. P. Walden, 2008: Dry bias in Vaisala RS90 radiosonde humidity profiles over Antarctica. *J. Atmos. Oceanic Techol.*, **25**, 1529–1541, https://doi.org/10.1175/2008JTECHA1009.1.

Sato, K., and N. Hirasawa, 2007: Statistics of Antarctic surface meteorology based on hourly data in 1957–2007 at Syowa Station. *Polar Science*, **1**, 1–15, https://doi.org/10.1016/j.polar.2007.05.001.

Schlosser, E., J. G. Powers, M. G. Duda, K. W. Manning, C. H. Reijmer, and M. R. van den Broeke, 2010: An extreme precipitation event in Dronning Maud Land, Antarctica: A case study with the Antarctic Mesoscale Prediction System. *Polar Research*, **29**, 330–344, https://doi.org/10.3402/polar.v29i3.6072.

Schmithüsen, H., 2020: Meteorological synoptical observations from Neumayer Station, 1981-01 to 2019-01, reference list of 457 datasets. PANGAEA, https://doi.pangaea.de/10.1594/PANGAEA.911242.

Schmithüsen, H., and H. Müller, 2019a: Radiosonde measurements from Neumayer Station (2018-11; 2018-12; 2019-01). Alfred Wegener Institute, Helmholtz Centre for Polar and Marine Research, Bremerhaven, PANGAEA, https://doi.org/10.1594/PANGAEA.900641.

Schmithüsen, H., and H. Müller, 2019b: Radiosonde measurements from Neumayer Station (2018-12). Alfred Wegener Institute, Helmholtz Centre for Polar and Marine Research, Bremerhaven, PANGAEA, https://doi.org/10.1594/PANGAEA.900642.

Schmithüsen, H., and H. Müller, 2019c: Radiosonde measurements from Neumayer Station (2019-01). Alfred Wegener Institute, Helmholtz Centre for Polar and Marine Research, Bremerhaven, PANGAEA, https://doi.org/10.1594/PANGAEA.900631.

Schmithüsen, H., S. Arndt, M. Nicolaus, M. Hoppmann, and C. Haas, S. Henning, and G. Heinemann, 2017: German contribution to YOPP-SH, Year of Polar Prediction in the Southern Hemisphere (YOPP-SH). *Proc. YOPP-SH Workshop*, Colorado, National Center for Atmospheric Research, Boulder, USA, https://doi.org/10013/epic.51386.d001.

Seefeldt, M. W., and J. J. Cassano, 2008: An analysis of low-level jets in the Greater Ross Ice shelf region based on numerical simulations. *Mon. Wea. Rev.*, **136**, 4188–4205, https://doi.org/10.1175/2008MWR2455.1.

Shields, C. A., and Coauthors, 2018: Atmospheric River Tracking Method Intercomparison Project (ARTMIP): Project

goals and experimental design. *Geoscientific Model Development*, **11**, 2455–2474, https://doi.org/10.5194/gmd-11-2455-2018.

Sinclair, V. A., and H. F. Dacre, 2019: Which extratropical cyclones contribute most to the transport of moisture in the Southern Hemisphere? *J. Geophys. Res.*, **124**, 2525–2545, https://doi.org/10.1029/2018JD028766.

Sodemann, H. and A. Stohl, 2013: Moisture origin and meridional transport in atmospheric rivers and their association with multiple cyclones. *Mon. Wea. Rev.*, **141**, 2850–2868, https://doi.org/10.1175/MWR-D-12-00256.1.

Souverijns, N., A. Gossart, I. V. Gorodetskaya, S. Lhermitte, A. Mangold, Q. Laffineur, A. Delcloo, and N. P. M. van Lipzig, 2018: How does the ice sheet surface mass balance relate to snowfall? Insights from a ground-based precipitation radar in East Antarctica *The Cryosphere*, **12**, 1987–2003, https://doi.org/10.5194/tc-12-1987-2018.

Stein, A. F., R. R. Draxler, G. D. Rolph, B. J. B. Stunder, M. D. Cohen, and F. Ngan, 2015: NOAA's HYSPLIT atmospheric transport and dispersion modeling system. *Bull. Amer. Meteorol. Soc.*, **96**, 2059–2077, https://doi.org/10.1175/BAMS-D-14-00110.1.

Sugidachi, T., and M. Fujiwara, 2013: Correction of the stepwise change observed at 0°C in Meisei RS2-91, RS-01G, and RS-06G Radiosonde relative humidity profiles. *J. Meteorol. Soc. Japan*, **91**, 323–336, https://doi.org/10.2151/jmsj.2013-306.

Sun, B. M., A. Reale, S. Schroeder, D. J. Seidel, and B. Ballish, 2013: Toward improved corrections for radiation-induced biases in radiosonde temperature observations. *J. Geophys. Res.*, **118**, 4231–4243, https://doi.org/10.1002/jgrd.50369.

Thyssen, F., and K. Grosfeld, 1988: Ekström ice shelf, Antarctica. *Annals of Glaciology*, **11**, 180–183, https://doi.org/10.3189/S0260305500006510.

Tomasi, C., and Coauthors, 2006: Characterization of the atmospheric temperature and moisture conditions above Dome C (Antarctica) during austral summer and fall months. *J. Geophys. Res.*, **111**, D20305, https://doi.org/10.1029/2005JD006976.

Tsukernik, M., and A. H. Lynch, 2013: Atmospheric meridional moisture flux over the Southern Ocean: A story of the Amundsen Sea. *J. Climate*, **26**, 8055–8064, https://doi.org/10.1175/JCLI-D-12-00381.1.

Turner, J. and S. Pendlebury, 2004: *The International Antarctic Weather Forecasting Handbook*. British Antarctic Survey, Cambridge, UK, 663 pp.

Turner, J., and Coauthors, 2019: The dominant role of extreme precipitation events in Antarctic snowfall variability. *Geophys. Res. Lett.*, **46**, 3502–3511, https://doi.org/10.1029/2018GL081517.

van Den Broeke, M. R., and H. Gallée, 1996: Observation and simulation of barrier winds at the western margin of the Greenland ice sheet. *Quart. J. Roy. Meteorol. Soc.*, **122**, 1365–1383, https://doi.org/10.1002/qj.49712253407.

van Den Broeke, M. R., and N. P. M. van Lipzig, 2003: Factors controlling the near-surface wind field in Antarctica. *Mon. Wea. Rev.*, **131**, 733–743, https://doi.org/10.1175/1520-0493(2003)131<0733:FCTNSW>2.0.CO;2.

van Den Broeke, M., G. König-Langlo, G. Picard, P. Kuipers Munneke, and J. Lenaerts, 2010: Surface energy balance, melt and sublimation at Neumayer Station, East Antarctica. *Antarctic Science*, **22**, 87–96, https://doi.org/10.1017/S0954102009990538.

van Lipzig, N. P. M., and M. R. van den Broeke, 2002: A model study on the relation between atmospheric boundary-layer dynamics and poleward atmospheric moisture transport in Antarctica. *Tellus A*, **54**, 497–511, https://doi.org/10.1034/j.1600-0870.2002.201404.x.

van Wessem, J. M., C. H. Reijmer, W. J. van de Berg, M. R. van den Broeke, A. J. Cook, L. H. van Ulft, and E. van Meijgaard, 2015: Temperature and wind climate of the antarctic peninsula as simulated by a high-resolution regional atmospheric climate model. *J. Climate*, **28**, 7306–7326, https://doi.org/10.1175/JCLI-D-15-0060.1.

Vignon, É., O. Traullé, and A. Berne, 2019: On the fine vertical structure of the low troposphere over the coastal margins of East Antarctica. *Atmospheric Chemistry and Physics*, **19**, 4659–4683, https://doi.org/10.5194/acp-19-4659-2019.

Vömel, H., D. E. David, and K. Smith, 2007: Accuracy of tropospheric and stratospheric water vapor measurements by the cryogenic frost point hygrometer: Instrumental details and observations. *J. Geophys. Res.*, **12**, D08305, https://doi.org/10.1029/2006JD007224.

Wille, J. D., V. Favier, A. Dufour, I. V. Gorodetskaya, J. Turner, J., C. Agosta, and F. Codron, 2019: West Antarctic surface melt triggered by atmospheric rivers. *Nature Geoscience*, **12**, 911–916, https://doi.org/10.1038/s41561-019-0460-1.

WMO, 2011a: Guide to climatological practices (WMO-100). World Meteorological Organization, Geneva. [Available from https://public.wmo.int/en/resources/library/guide-climatological-practices-wmo-100].

WMO, 2011b: Manual on Codes-International Codes, Volume I.1, Annex II to the WMO Technical Regulations: Part A—Alphanumeric Codes, WMO No. 306. World Meteorological Organisation, Geneva. [Available from https://library.wmo.int/index.php?lvl=notice_display&id13617#.XmX-cAPmj7wA].

Yamada, K., and N. Hirasawa, 2018: Analysis of a record-breaking strong wind event at Syowa Station in January 2015. *J. Geophys. Res.*, **123**, 13 643–13 657, https://doi.org/10.1029/2018JD028877.

Yamanouchi, T., M. Fukuda, H. Ogihara, K. Kawashima, and M. Doi, 2020: Meteorological synoptical observations from station Syowa, 1994-01 to 2019-01, reference list of 300 datasets. PANGAEA. Available from https://doi.pangaea.de/10.1594/PANGAEA.911265.

Zhu, Y., and R. E. Newell, 1998: A proposed algorithm for moisture fluxes from atmospheric rivers. *Mon. Wea. Rev.*, **126**, 725–735, https://doi.org/10.1175/1520-0493(1998)126<0725:APAFMF>2.0.CO;2.